UNIVERSITÀ
DEGLI STUDI
FIRENZE
DIEF
DIPARTIMENTO
DI INGEGNERIA
INDUSTRIALE

Department of Industrial Engineering

PhD School in Industrial Engineering
PhD in Energy Engineering and
Innovative Industrial Technologies
XXVI cycle (2011-2013)

A redesign strategy for high-pressure steam turbine stages

Settore Scientifico Disciplinare ING-IND/09

PhD student: Juri Bellucci

Supervisor: Prof. Andrea Arnone
Co-supervisor: Dr. Filippo Rubechini
Co-supervisor: Dr. Arcangeli Lorenzo

Coordinator: Prof. Maurizio De Lucia

Florence, December 2013

[...] Reagiamo pure noi
Chiediamo di più
Che sia davvero un mondo onesto.
Ognuno faccia il suo
Passione ed energia
Sbagliare in fondo serve tanto.
L'avidità ci impoverisce
Gli slanci invece no
Se quell'istinto si perdesse
Dove troverebbe le risposte
Questa vita chi lo sa. [...]

– Renato Zero

Dedicated to my parents
and Sabrina

Desidero ringraziare innanzitutto il Prof. Ing. *Andrea Arnone*, per avermi dato la possibilità di svolgere questo importante percorso all'interno del suo gruppo di ricerca.

Un ringraziamento particolare va al Dr. *Filippo Rubechini*, per avermi seguito durante questi tre anni trasmettendomi la passione e l'entusiamo per questo lavoro. Grazie per i preziosi consigli che hai saputo darmi e per essere stato oltre che uno stimato collega anche un amico.

Sono in debito anche con il Dr. *Lorenzo Arcangeli*, di GE Oil&Gas, per l'esperienza e la conoscenza che ha portato con il suo supporto tecnico.

Grazie a tutti "i ragazzi" del *T-Group*, Lorenzo, Matteo G., Matteo C., Ettore, Francesco, Federica, Michele, Andrea e Roberto non solo per la competenza e la professionalità, sulle quali ho potuto sempre contare, ma anche per l'amicizia che mi hanno dimostrato: grazie per aver condiviso insieme a me passioni, gioie ed amarezze...

Un grazie speciale va a *Sabrina*, insostituibile compagna. Accanto a te tutto sembra più leggero, colorato e vivo, grazie per avermi sostenuto e incoraggiato e per avermi insegnato a vedere il mondo con "occhi diversi".

Per ultimi, ma non certo per importanza, ringrazio con tutto il cuore i *miei genitori*, maestri e punti di riferimento della mia vita. Grazie a voi ho potuto intraprendere questo percorso, vivere un'entusiasmante avventura e raggiungere un importante traguardo. Non dimenticherò mai quello che mi avete insegnato.

Introduction

In the industrial design of turbomachinery, a key factor is represented by time-to-market. The strong competition among turbomachinery companies to satisfy customer requirements and the more and more stringent environment regulations, pushes towards the design of compact machines with high efficiency and reliability, and reduced costs. The efforts and the resources to employ in redesigning a whole machine, starting from scratch, does not meet generally the time requirements of a market strategy. This leads to face the issue of splitting the main redesign problem in smaller, easier to manage, problems in order to reduce time and costs while preserving competitiveness. For these reasons, the aerodynamic as well as the mechanical redesign of a single component become a key aspect.

Nowadays, a redesign problem is often a multidisciplinary issue, which involves simultaneously aerodynamic as well as aero-mechanical and heat transfer aspects. The geometries of the components have complex three-dimensional features always more difficult to manage with simple and standard one-dimensional approaches based on empirical correlations. Moreover, the customers requirements aim to obtain a reliable and flexible product able to work in the whole operating envelope of a plants. Thus, due to the huge amount of informations that should be concurrently taken into account to meet all the requirements to design a new line of products,

it is easy to understand the need for the designer to employ a modern computer-based redesign procedure to obtain an optimal solution in a reasonable time.

All these considerations are enough to explain the industrial interest in pushes the researcher for a continuous improvement of these tools towards automatic and effective procedures for multidisciplinary design. The emphasis is justified by the capability of these optimization algorithms to exploit the great amount of information provided by numerical simulations, and correlate them to the geometrical parameters in order to find their optimal combinations.

The main topic of this PhD thesis is the description and the analysis of a redesign strategy for high-pressure steam turbine stages. The overall procedure will be presented, from the choices made for the stage optimization to the numerical verifications need for the new product industrialization. The optimization technique relies on a response surface method, coupling the high-fidelity CFD RANS computations with an optimization algorithm based on meta-models. The emphasis will be mainly focused on two meta-models in particular, the support vector machines and the artificial neural networks: an entire chapter will be devoted to their description, and a comparison between these two methodologies will be reported in the section concerning the results of the stage optimization. A wide section will be devoted to the impact of surface roughness, since it is a relevant and active research area and it plays a role of main importance into blades design.

Contents

List of Figures

List of Tables

Nomenclature

A	Area
AR	Aspect Ratio $= h/c$
b	Bias term
C_f	Skin friction coefficient, $C_f = \tau_w/(^1/_2\rho u^2)$
c	Chord, absolute velocity
d	Desired output
DR	Diffusion Rate $= \frac{M_{max}/M_{TE}-1}{1-s_{max}/s_{TE}}$
H	Enthalpy
Err	Training set relative error
e	Error variable
h	Blade height
J	Principal moment of inertia
k	Turbulent kinetic energy
k_ℓ	Laminar kinetic energy
$\mathrm{K}(x_i, x_j)$	Kernel function
k_s	Equivalent sand grain roughness height

k_s^+	Roughness height in wall units, $k_s^+ = k_s v^*/\nu$
ℓ_T	Turbulence length scale, $\ell_T = k^{1/2}/\omega$
M	Mach number
m	Deviation
N	Rotational speed
O	Output of neuron
p	Pressure
PR	Pressure Ratio $= p_{01}/p_{s2}$
R_y	Wall-normal-distance Reynolds number, $\sqrt{k}y/\nu$
r	Radius
Re_{k_s}	Roughness Reynolds number, $Re_{k_s} = Rek_s/c$
Re	Reynolds number, $Re = {}^{u_2 c}/_{\nu}$
RR	Radius Ratio $= r_{tip}/r_{hub}$
R_t	Peak-to-valley roughness
S	Mean shear rate $S = \sqrt{2S_{ij}S_{ij}}$
s	Curvilinear abscissa
Tu	Turbulence intensity, $Tu = \sqrt{{}^2/_3\ k}/u$
T	Temperature
u	Velocity magnitude, blade speed
v^*	Friction velocity, $v^* = \sqrt{\tau_w/\rho}$
w	Weights vector
x	Input data, cartesian coordinate

y^+	Distance from the surface in wall units, $y^+ = yv^*/\nu$
Y	Total pressure loss
y	Output data, cartesian coordinate
Z_w	Zweifel number

Greek:

α	Momentum term, weight of G.E.M. method, blade-to-blade flow angle
ξ	Stagger angle (from axial)
δ_Ω	Shear layer vorticity thickness, $\delta_\Omega = \frac{u_\infty}{2}\left(\frac{\partial u}{\partial y}\right)^{-1}_{\max_y}$
Δ	Variation
$\Delta\eta$	Efficiency variation
η	Learning rate, stage total to total efficiency
γ	Regularization term
λ	Lagrange multiplier
ν	Neuron activation, kinematic fluid viscosity
ω	Specific turbulence-dissipation rate
ϕ	Transferring function, flow coefficient $= c_{ax}/u$
ψ	Work coefficient $= \Delta H_0/u^2$
ρ	Density
σ	Kernel hyper-parameter
τ_w	Wall shear stress
ζ	Enthalpy loss coefficient

Subscripts and undersigns:

0	Total
1	Inlet section
2	Outlet section, bucket exit
ax	Axial direction
cr	Critical
∞	Free-stream
is	Isentropic
ℓ	Laminar
max	Maximum
min	Minimum
p	Profile
ref	Reference value
sec	Secondary
smooth	Smooth surface
s	Static
T	Turbulent
TE	Trailing edge
th	Threshold
tot	Total (inlet-outlet section)
w	Wall value

Acronyms:

ANN	Artificial Neural Network
CFD	Computational Fluid Dynamics
FT	Fully Turbulent
LKE	Laminar Kinetic Energy
MSE	Mean Square Error
OF	Objective Function
SVM	Support Vector Machine

Chapter 1

Redesign strategy

In this chapter a brief description of the redesign strategy employed in this work will be reported. After some general consideration on the steps usually involved in such a methodology, the key aspects of each step will be analysed critically.

1.1 General consideration

With respect to some decades ago, the approach of the designer to the aerodynamic and mechanical redesign of a turbomachinery component is changed. Many often the requirements of the customer involve to investigate a component with complex three-dimensional geometry and to test it in different operating condition simultaneously, with the scope to optimize the performance under stringent constraints. To solve such a multidisciplinary problem is need to explore a wide design space and consider tens of variables to find their better combination, in order to satisfy all the targets. This make the work of the designer very hard for both time-consumption and satisfaction of the obtained results.

These industrial needs have been the spring that have pushed into the development of computer-based design tech-

niques. These driven the designer into research an optimal solution of such problems, in a reasonable time and with good results.

Many often, such an approach couple the high-fidelity results of the computational fluid dynamics (CFD) simulations, with the capability of optimization algorithms to manage the great amount of informations contents in these data. The algorithms "replace" the work of the designer, employing these informations to find an optimal geometrical configuration which respects the objectives and the constraints of the problem studied.

A redesign procedure is generally composed by different phases, generally split up in four main steps: parametrization of the geometry, sampling of the design space, CFD simulations, and thorough research of a optimal solutions set. Each step plays an important role into achieve a good optimization result. As far as parametrization is concerned, many efforts have been done during the last decades to improve it, achieving a high-level of maturity. Different approaches were proposed in order to ensure an easy and robust handling of blades and meridional flow paths geometries, for axial as well as centrifugal turbomachines (Chen and Yuan [1], Burguburu and le Pape [2], Checcucci et al. [3], Pritchard [4]). These generally employ parametric curves (Bézier, B-splines or N.U.R.B.S.) to describe the component to study (Fig. 1.1). Often, the control points of the curves are related each one, in order to directly handling the main geometrical features of the component. The sampling of the design space is by now guided by means of quasi-random sequence (e.g. latin hypercube, Sobol's sequence, hypersphere, etc.), that are simple to manage and allow to avoid samples clustering (Fig. 1.2). Thinking that the CFD computations can not be entirely replaced by any other tool although their time consumption (however more and more reduced by using multi-core cluster), the weak link of the overall procedure seems the optimization algorithm. Nowadays many different strategies can

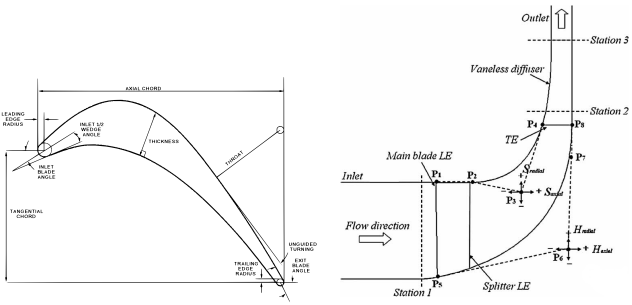

Figure 1.1: **Examples of parameterization**

be cited and classify in categories, basing on the different features or the integration level with the coupled CFD code that each one have: such as gradient methods, methods based on the response surface approximation (e.g. ANN, D.O.E.), exploratory techniques (e.g. Genetic Algorithm, Simulated Annealing), adjoint method etc. (Rubechini et al. [5], Bonaiuti et al. [6], Leung and Zingg [7], Van den Braembussche et al. [8], Ellbrant et al. [9], Chahine et al. [10]). Each one shows advantages and drawbacks, depending by the number of degrees of freedom, the multi-dimensions design space shape, e.g. convex, continuum etc., the number of calculations required, the level of problem approximation. This wide possibility of choice for the end users, point out that during the years no one of the proposed methods is resulted better than others. Thus, in the author's opinion is here that is necessary to spend a lot of efforts, in order to improve the whole optimization process.

Among the vary strategies, the methods based on the response surface seem have reached a good level of maturity and represent a good compromise in terms of time-consumption and prediction accuracy. They are suitable for optimization problem where the design space has a complex multi-peak

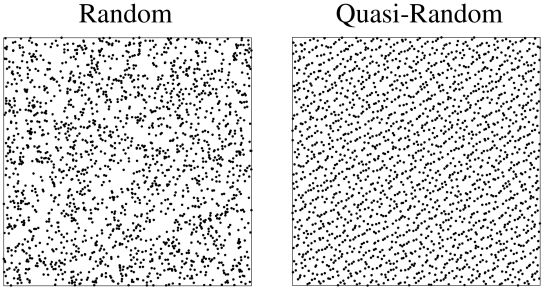

Figure 1.2: **Examples of design space sampling**

shape and many geometrical parameters have to be taken into account. An example of optimization cloud is shown in Fig. 1.3 where stage efficiency is plotted against mechanical constraints. Recently a novel approach to rebuild the response surface of an optimization problem was employed: the support vector machine (SVM). The characteristics of such an approach have allowed its use in very different scientific fields, from defect diagnostics of steam and gas turbines, to environmental or medical applications. It was used as classifier or in regression mode and sometimes was applied within an hybrid structure together with artificial neural network or genetic algorithm.

Seo et al. [11] employed an hybrid SVM-ANN to diagnostic the defects of a gas turbine engine, pointed out the reliability of the diagnose predicted. Lu and Wang [12] assessed the feasibility of use a SVM approach to monitoring the air pollutant level into the atmosphere. The results obtained were compared with those of an RBF network, pointed out the better prediction accuracy of the SVM approach. Adankon and Cheriet [13] applyed a least-square support vector machine to handwriting recognition showing the usefulness of this model as classifier and the importance of the hyper-parameters selection. Anguita et al. [14] used a SVM for the aerodynamic

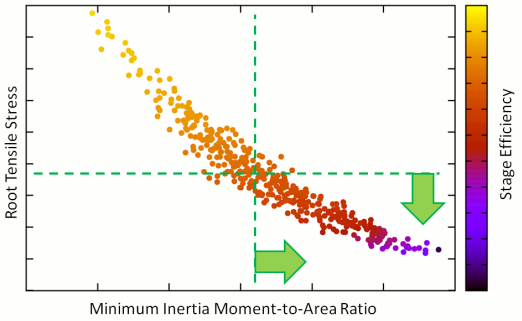

Figure 1.3: **Example of an optimization cloud**

design of the blade profile of a turbine cascade. The meta-model was used in regression mode to solve a bi-dimensional problem with sixteen degrees of freedom and two objective function (outlet flow angle and total pressure loss coefficient).

Once an optimal solution is found some verifications, in different configurations from the one/ones studied during the optimization, have to be carried out. Usually in this phase can be defined a matrix of calculations in which the main loss sources are investigated, such as profile, secondary and leakage losses (following an historical classification). To this end, the parameters that play a significant role in affecting these losses are varied in a range of practical interest. Depending on the specific application can be considered parameters such as aspect ratio (AR), radius ratio (RR), stagger angle, robustness to incidence, pitch to chord ratio, blade size and count ratio, surface roughness, leakage mass flow and so on. As a results, such verifications provide a big picture of the advantages and drawbacks derived from the use of the optimized geometry. Thus allowing its industrialization within the design chain and the fine tuning of the preliminary design tools.

1.2 Optimization procedure

In this work, the redesign of the high-pressure steam turbine stage has been carried out by means of the following strategy. The adopted approach is similar to that proposed by Pierret and Van den Braembussche. [15], which involve CFD analyses and a response surface method for the optimum selection.

The overall procedure is composed of several steps:

- geometry parametrization
- sampling of the design space
- CFD runs of each sample
- response surface generation
- CFD verification of optimal solution

A powerful and versatile parametrization is one of the key aspect of the blade optimization. In this work the three-dimensional blade geometry was handled by using a parameterization based on Bézier curves. The use of such approach, to describe the airfoil and the span-wise distribution of all airfoil parameters, ensure good and accurate reproduction of the blade shape, moving a limited set of significant parameters.

The design space was defined once the parameters subjected to optimization and their variation range were selected. A low-discrepancy sequence was used to populate the design space, in order to have a more uniform sampling, and make the training of the meta-model more efficient. Then, the corresponding geometries were calculated.

A meta-model was used to generate an approximate response surface for each objective function (OF) and constraint. Usually an artificial neural network is employed, and is reliability has already tested in different applications (Rubechini et al. [16] and [5], Checcucci et al. [3]). In this work the author propose to use a novel meta-model for the aerodynamic design of turbomachinery blade: a support vector

machine. The type used was a least-square SVM and it was employed in regression mode. More details will be given in the next chapter while a comparison with the ANN approach will be discussed in chapter 4.

Finally, a set of optimal geometries suggested by the meta-model, which satisfy objective functions and constraints, were verified through numerical simulations, leaving to the designer experience the choice of the final solution.

Once an optimal solution is found, some verifications are planned in different configurations from the one/ones studied during the optimization. According to the industrial design rule, a matrix of additional calculations is defined identifying those parameters that affect the main sources of loss. For the present case, a detailed analysis of the effects of surface roughness will be carried out. Finally, the impact of stagger angle, AR, RR and shroud leakages on stage performance will be investigated.

Chapter 2

Meta models

In this chapter the description of the features of two meta-models will be reported and discussed in details. First, the novel approach proposed in this work, the support vector machine, will be described and the parametric analysis carried out to proper select the hyper-parameter will be discussed. Finally, a widely used meta-model, the artificial neural network, will be presented and different training methodology will be analysed.

2.1 Support vector machine

2.1.1 Some background information

The support vector machines (SVM) has been developed at the end of the nineties from Vapnik et al. They are based on the support vector algorithm, generalization of the generalized portrait develop from Vapnik et al. (about sixties). It is framed into the statistical learning theory (Vapnik - Chervonenkis theory), which characterized the learning algorithms property, allowing them to generalize to new data the elements prior learned.

As learning method, the support vector algorithm is able to generate an approximate function of the response surface of the problem, starting from a set of input/output parameters (training data), in classifier and regression mode. An important aspect in the SVM approach is how the approximation function is sought. Generally this problem is related to find the best function that minimize the empirical risk. As commonly used into statistical machine learning or to train an artificial neural network, using a typical loss function such as squared error or absolute value error. The SVMs formulation instead is based on a different approach following the structural risk minimization. This is a key aspect for the learning, because it aims to minimize the generalization error admitting some lack into training data set approximation.

The support vector machines can work with linearly separable and non-separable data in "N"-dimensions. In practice the training algorithm try to seek the optimum hyperplane separator that maximize the distance between the training samples closest to this plane and the plane itself. This problem can be solve with the Lagrange multipliers technique, where the generic multiplier, λ_i, is obtained by solving a quadratic programming problem. Each input parameter that has the corresponding λ strictly greater than zero is called support vector. These are the critical samples of the training set and most close to the optimum hyperplane. This procedure, briefly described, can be used for linearly separable and non-separable data, introducing slack variables for the not-separable case and admitting, in this second case, a certain tolerance to the errors.

For problems with separable or non-separable non-linear data, the same procedure early described can be employed by mapping the initial non-linear "N"-dimensions input parameters in a new space with higher dimension, called feature space: in this space the data are again linearly separable or non-separable. Then a kernel function is introduced within the optimization algorithm, to avoid numerical instability and

higher computational time with respect to the linear case.

In this work a least-square SVM was employed, this type of machine is computationally more efficient than the standard SVM method, because the training algorithm treats linear equations instead to solve a quadratic programming problem. On the other hand, this simplification reduced the sparseness capability of the machine, that can be restore, almost partially, using different methods.

The decision function found by the LS-SVM is in the form:

$$f(x) = sign[w^{'}\phi(x_i) + b] \tag{2.1}$$

where w and b are determined by solving the following optimization problem to minimize the training error and find the optimum hyperplane:

$$\text{minimize} \quad \frac{1}{2}w^{'}w + \frac{1}{2}\gamma\sum_{i=1}^{N} e_i^2 \tag{2.2}$$

$$\text{subjected to} \quad y_i - w^{'}\phi(x_i) - b = e_i \quad \forall i = 1, ..., N \tag{2.3}$$

where w is the weight vector, γ is the regularization term which determines the trade-off between the model complexity (flatness) and the training error, e_i are the error variables, y_i are the output data, $\phi(x_i)$ is the function which maps the input data into a so-called higher dimensional feature space, and b is the bias term. The introduction of a squared loss function into the objective function and an equality constraint into the second equation, make the problem to solve linear.

Some more details about how to solve the optimization problem, which technique can be used to improve the robustness and the sparseness of the machine, can be found in Suykens et al. [17, 18] and Valyon [19]. Moreover, more details involving the training algorithm formulation and a wider bibliography, can be found within more specialist work on this topic, such as Vapnik ([20],[21]), Burges [22], Smola and Schölkopf [23] and Cherkassky and Ma [24].

2.1.2 Hyper-parameters selection

Once the optimization problem is formulated mathematically (represented by the equations system (2.2) and (2.3)), a good setting of γ and the kernel parameters is need to get the better SVMs generalization performance. The impact of the regularization term on the solution of the optimization problem can be pointed out from the figure 2.1, where the LS-SVM was used to approximate the function (2.4), employing the training dataset composed by the open squares.

$$y(x) = \frac{sin(x)}{x} \tag{2.4}$$

Among the different kernel functions that can be adopted to map the input samples in the feature space, the stronger regularized universal Fourier kernel function was employed, defined by the following equation:

$$K(x_i, x_j) = \frac{1 - \sigma^2}{2(1 - 2\sigma cos(x_i - x_j) + \sigma^2)} \quad 0 < \sigma < 1 \tag{2.5}$$

Figure 2.1 shows several approximation functions generated by setting different values of the regularization term γ ranging from 10^1 up to 10^4, held fixed any other parameter. The figure highlights as the increase of γ reduce the flatness and arise the complexity of the response surface predicted, in order to obtain a better approximation of the function $y(x)$. This result do not means that the value of γ has to be greater as possible, because a major complexity often implies a worse generalization performance. The effect is more or less marked depending on the studied problem: in particular from the samples that compose the training set and the shape of the response surface to generate. The great variability of the parameter and the corresponding predictions makes the selection of this factor very important into research the right solution of a specific problem.

Similar conclusions can be draw for the kernel parameters. Using the Kernel function represent by the equation (2.5),

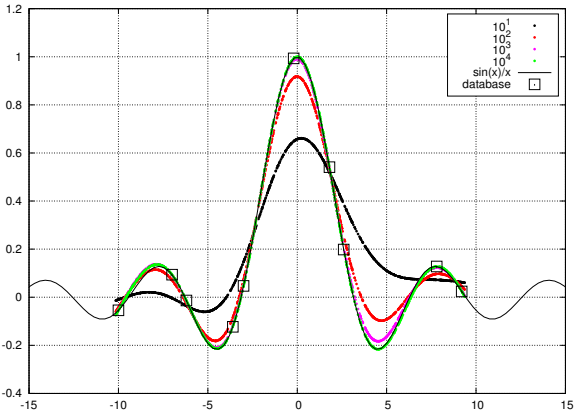

Figure 2.1: **Impact of regularization term γ on the solution flatness**

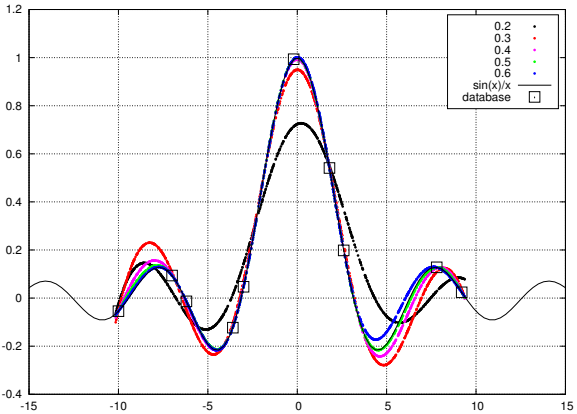

Figure 2.2: **Impact of kernel parameter σ on the approximation function**

the only hyper-parameter to set is σ. Figure 2.2 summaries the results obtained by setting different values of σ ranging from 0.1 up to 0.6, for a fixed value of γ. With respect to γ values, the range of σ is very narrow and the variability of the response surface generated is wide. Moreover there is not a regular trend towards a better approximation of the function to fit. This makes any conclusion on the trade-off between training and generalization capability difficult to get from this simple analysis. Thus, the selection of this parameter has to be made with more careful that for the γ value, due to its strong impact on the solution found.

These few considerations, get from this simple case, are enough to sensitize the reader to the importance of a right selection of the hyper-parameter and to justify a parametric analysis. This one was performed in order to set γ and σ to employ for a complex class of problems with many input and output variables, such as the aerodynamic redesign reported in the next chapter.

The first step of the parametric analysis was to create a database representative of such an optimization problem in order to train the LS-SVM. A design space generated by varying eleven input parameters in a specific range was selected. The sampling of the space was performed using a quasi-random sequence, rather than a random sampling, to ensure a well determined statistical distribution of the new geometries in terms of mean value and variance. Moreover, all the input parameters are non-dimensional between -1 and 1. The variables selected allow to handle the three-dimensional geometry of a blade row and are typical for both axial and centrifugal machines, such as inlet and exit angles, thickness distribution etc. For each geometry, a three-dimensional RANS calculation was performed in order to evaluated three objective functions (output variables for the SVMs), again commons for both axial and centrifugal machines, such as efficiency, mass flow rate and work coefficient (hereafter referred as OF1, OF2 and OF3).

The database created in this way is representative of an aerodynamic redesign problem, making the tuning of the SVMs hyper-parameters suitable for other optimization problems of this type.

Once the database was created, the impact of γ and σ value on the fitting and generalization error was investigated in a wide bi-dimensional space ranging from $1.0\text{x}10^1$ up to $1.0\text{x}10^6$, for the first parameter, and from 0.1 up to 0.7 for the second one. The LS-SVM was trained using about 1800 examples to compound the fitting data set (hence to train the machine) and about 200 for the generalization one. The results of such an analysis is presented severally for each parameter, by cutting the studied surface at a constant value of the other variable. This allow to show the informations content into the results in a more clear way. First, the impact of γ was analysed. Figure 2.3 and 2.4, show the trends of the fitting and generalization error, calculated by means of (2.9). Here the errors were reported with respect to γ for each objective functions:

$$Err(y) = \frac{\sum_{i=1}^{N} |y_{i_{CFD}} - y_{i_{SVM}}|}{N} \tag{2.6}$$

The fitting error shows a monotonous decreasing trend with the rise of the hyper-parameter for each OF considered, suggesting the use of a very high value of γ to have the lower error. The same conclusions was previously found analyzing the impact of hyper-parameters for the function reported into the equation (2.4). Similar considerations can be draw analyzing the trend get for the generalization error. Now the curves are almost flat and present a minimum value when γ is about $5.0\text{x}10^3 \div 1.0\text{x}10^4$, depending from the objective function choose. Thus taking a γ value of about $1.0\text{x}10^4$ seems guarantee the better generalization performance of the LS-SVM. Nevertheless, in the experience of the authors, seem that the better performance of the meta-model in terms of quality of the approximated response surface generated, is

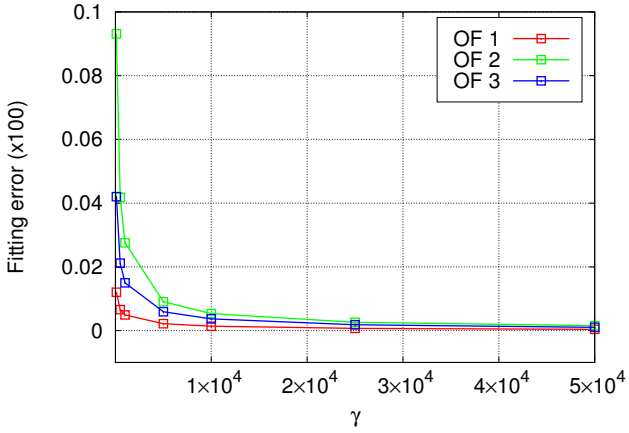

Figure 2.3: **Trend of fitting error with respect to γ value**

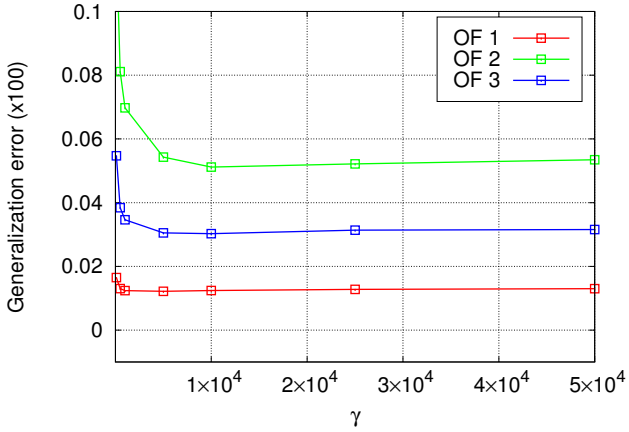

Figure 2.4: **Trend of generalization error with respect to γ value**

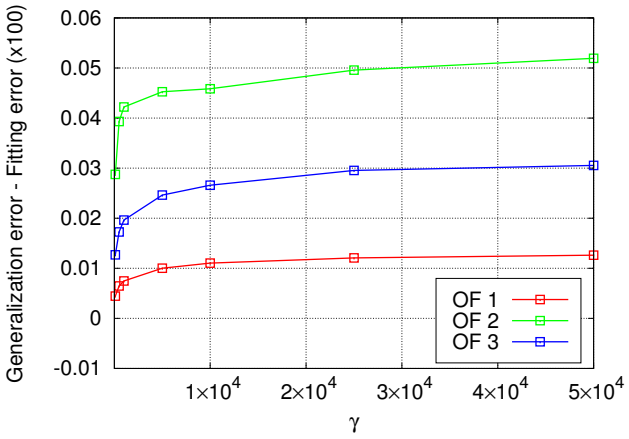

Figure 2.5: **Trend of the difference between generalization and fitting error with respect to γ value**

reached when the two errors, fitting and generalization, are close among them and produce a low error.

Bearing in mind this consideration, with referring to figure 2.5 where the curve that represent the difference between the two errors are shown, a γ value of about $1.0\text{x}10^3$ was selected. This value will be employed in the optimization problem described in the next chapter. It is worth noticing that to summarized the results for all the OF in a single figure, the selection of the scale of the y-value modify the actual shape of the curve. This hide to the reader that the variation between the maximum and the minimum error can ranging from about 20% to 50%, depending on the function, making important the impact on the response surface rebuilding.

Once chosen the value for γ, the impact of σ was studied. The trend of the fitting and generalization error with respect to σ are shown in figure 2.6 and 2.7 for each of the three objective functions. Respect to the γ analysis, two different

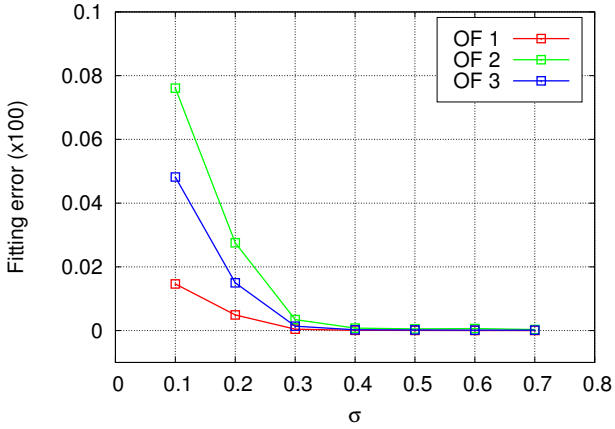

Figure 2.6: **Trend of fitting error with respect to σ value**

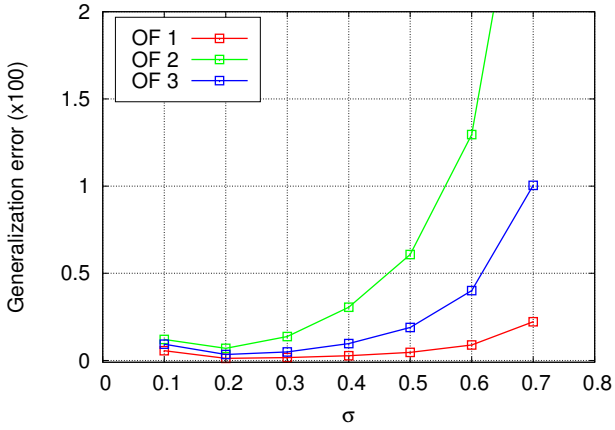

Figure 2.7: **Trend of generalization error with respect to σ value**

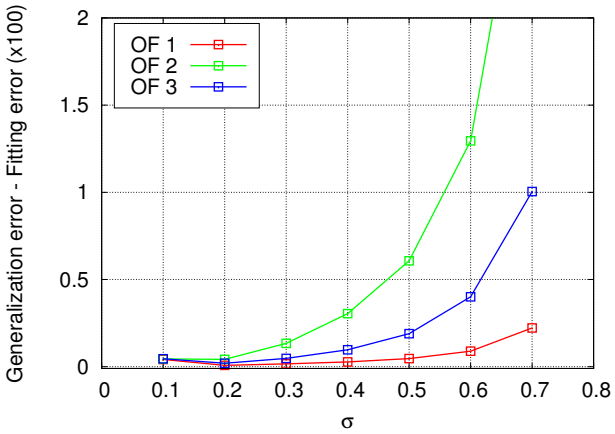

Figure 2.8: **Trend of difference between generalization and fitting error with respect to σ value**

trend were identified for the errors, a monotonic decreasing for the fitting and a quasi-parabolic with an optimum value for the generalization one. The choice of the right value, in accordance with the previous study, was made by checking the difference among the two errors. Thus, a value of $\sigma = 0.1$ seems represent the better trade-off for each objective function and therefore was selected and used during the redesign presented later. Again, as for the γ analysis, the scale of the y-value of the graphs hide the high variations of the hyper-parameter with respect to σ value, that in this case can reach one order of magnitude.

It is worth to note as the narrow range of variations of σ with respect to γ imply a more careful selection. Its optimal value can be slightly vary from a problem to another, while the value of γ is certainly more stable and reliable to different redesign applications.

2.2 Artificial neural network

2.2.1 Some background information

An artificial neural network (ANN) is a dynamic system which tries to reproduce the way of work of the neural network of human brain. This can be compared to a high-complex, non-linear and parallel computer. Its base unity is the neuron, and the information that two or more neurons exchange between them is weighted by the strength of the synaptic connections: here is contained all the knowledge acquired. Thus an ANN is a system based on simple process unit, which elaborate the data of a determine problem in parallel, and store into the strength of neural connection the knowledge acquired during a training process. Such a knowledge will be exploit to find a new solution when a never seen input is used to interrogate the network. This architecture allow to solve non-linear and complex problems, hard to simple manage with other methods.

Considering a generic network topology (Fig. 2.9), a k-neuron incoming input consists of the outputs (O) of the m unities linked to it and weighted by the strength of the synaptic connection w_{km} between the unity k and m. The sum of these weighted inputs represent the neuron activation ν_k (2.7): the corresponding neuron output will depend by the transferring function ϕ adopted (2.8). The most use are the *sigmoid* and *hyperbolic tangent*.

$$\nu_k = \sum_m w_{km} O_m \tag{2.7}$$

$$O_k = \phi(\nu_k) \tag{2.8}$$

The value of the weights of each synaptic connection is determined by the network training. In this phase, a series of input/output couples is provided to the network in order to make it able to re-build the shape of the response surface of

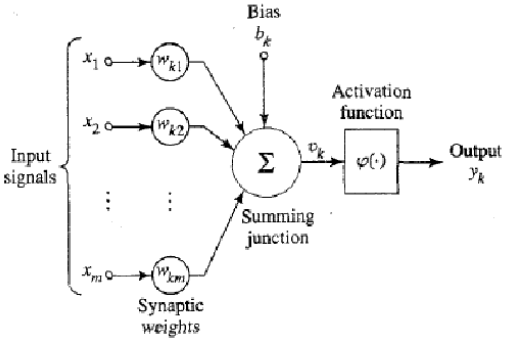

Figure 2.9: **Example of artificial neuron structure**

the problem. In practise, during the training it has to find the right values combination of all the synaptic connections.

From a mathematical point of view the training process consists in to research the minimum of an error surface in N-dimensions. The more easy and robust method employed exploit the gradient descent technique, which base the weights correction on the first order derivative of the error surface. Others technique which are based on second order criteria, needs of more stringent conditions to be applied and are more complex to implement, thus are not widely used. The training procedure consist in to run the network using the inputs available, compare the results with the desired output and compute the error made (generally a quadratic error):

$$e = \frac{1}{2}\sum_k (d_k^2 - y_k^2) \tag{2.9}$$

Then the value of the weights is corrected according to the gradient descent technique.

$$\Delta w_{km} = -\eta \frac{\partial e}{\partial w_{km}} \quad \text{with} \quad 0 < \eta < 1 \tag{2.10}$$

where η is the learning rate. The procedure is iterative and is repeated until the mean error made on the whole set of input reach the desired value. It is important to find the better combination of the weights in which way these are initialized. This can affects the global time of the training and favour an early neurons saturation. A generic initialization of the weights matrix suggest to have a null mean value and a variance equal to the square root of the synaptic connections. The training procedure described is call *supervised*. Generally the training set is split up in two database: the first is call *fitting* set, composed of about $80 - 90\%$ of the total training set, while the second is call *validation* set. The first database is used to train the network, while the second one is employed to verify the generalization capability acquired during the training. The network never seen this last set of example during the training. Thus the resulting outputs predicted for this database is only dependent by the accuracy of the response surface re-building. A key factor to have a high accuracy of the response surface approximation is provide a significant set of example well representative of the problem to study.

In this work a simple feed forward network with two hidden levels was used. According to Hecht-Nielsen theorem, this structure of the network is able to compute any function $F(x)$ with a certain accuracy. A gradient-based back-propagation algorithm was employed for the training. The method consists in two steps. In the first one, the network is run employing all the example of the fitting database and the error made is calculated. Then, in the second step the weights correction is performed by propagating the error to back. Thus the layer close to the output are the first to be corrected and so on for all the other layers. In order to speed up the learning, a *momentum* term (α) has been implemented into training algorithm. Moreover, in order to improve the generalization capability, ten neural network with different architectures and weights initialization were adopted for an effective hybridization.

More details concern the network typology, training algorithm formulation and hybrid networks can be found in [25, 26, 27, 28].

2.2.2 Learning rate and momentum term

As discuss for the support vector machine case, a key factor to have a good training of the meta model is the set up of all the coefficients involve in the training phase. For the ANN two are the parameters to be set: the learning rate and the momentum term.

As in the case of the SVM hyper-parameters selection, the same database (fitting as well as validation) representative of an aerodynamic redesign problem was selected. With respect to the SVM case, all the input parameters were non-dimensional between 0 and 1, according to the definition limit of the *sigmoid* transferring function. Moreover, the same objective functions, that is the output variables, and were selected.

First looking at the effect of learning rate on training. This coefficient determine the training speed up and convergence, with minor impact on the generalization capability. The higher is its value and the higher is the weights correction. The effect of the learning rate is to do swing the weights values on the error surface until a minimum of the function is reached. From one hand, high η allows to have a quick training but no-convergence of the process is possible, that is a higher generalization error or an over-training of the network can be reached. On the other hand, low η ensures the convergence of the training but the risk to find a relative minimum is higher. The result depend on the case. Figure 2.10 shows the trend of fitting error by varying the learning rate value between 0.1 and 0.9: for the sake of clarity only three curves are reported. An increasing of η speed up the learning mainly in firsts phases of the process, and as a result the target error is reached more quick. As aforementioned, this do not always correspond to a training convergence. In fact, looking at fig-

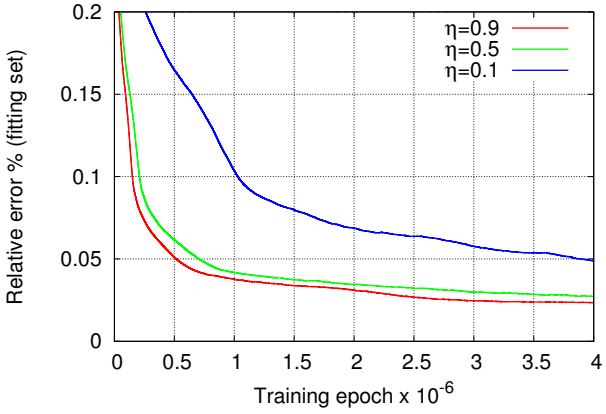

Figure 2.10: **Impact of learning rate on ANN fitting error**

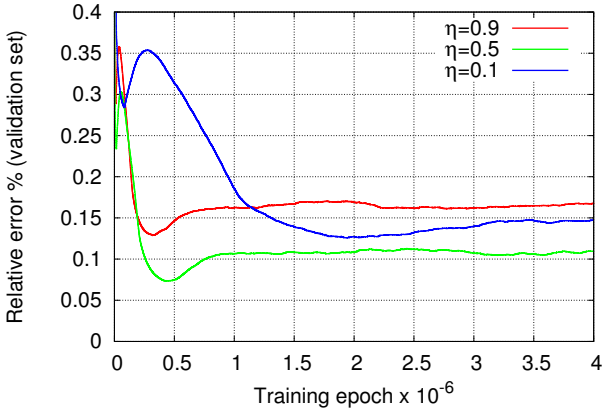

Figure 2.11: **Impact of learning rate on ANN generalization error**

ure 2.11, for the higher η results the higher generalization error. Analysing the two plot, a value of $\eta = 0.5$ seems reasonable to speed up the training and improve the prediction capability of the network.

A simple way to increase the training stability at higher learning rate is introduce a *momentum* term (α) in the weights correction formula:

$$\Delta w_{km} = f(\alpha, \Delta w_{km-1}) \quad \text{with} \quad 0 \leq \alpha < 1 \tag{2.11}$$

The effect of this term is to increase the weight correction when the partial derivative, calculate for the example n, has the same sign of the one calculate for the example $n-1$. While, in the case that the two derivatives have opposite sign the correction Δw_{km} is reduced. Thus, the training process is more quick ans stable. Quicker, because when the two derivatives have the same sign, it means that the gradient vector is moved in the right direction toward the minimum of the error surface. To correct the weight of a bigger quantity cause a rapid achievement of the optimum value of w which minimize the error of network output. Moreover, the training in more stable because when the two derivatives have opposite sign, the weight is less corrected and the oscillation of the network over the error surface is smaller with respect to the case with $\alpha = 0$. Figure 2.12 and 2.13 show the trend of fitting and validation error by varying α in a range from 0.0 to 0.9, held fixed $\eta = 0.5$: as for η analysis only three curves are reported within the plots. Analysing them it can be point out that the same fitting error is obtained with a reduced number of epochs and the generalization capability is improved. As a result, a value of $\alpha = 0.7$ seem reasonable for the present application.

2.2.3 Hybrid neural networks

An hybrid neural network is a system formed by more network which work in parallel, and in which the outputs are

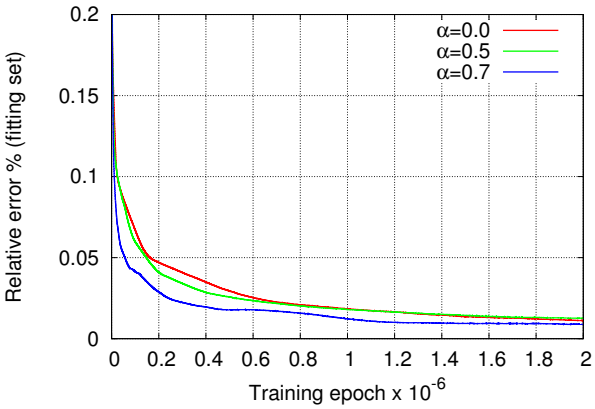

Figure 2.12: **Impact of momentum term on ANN fitting error**

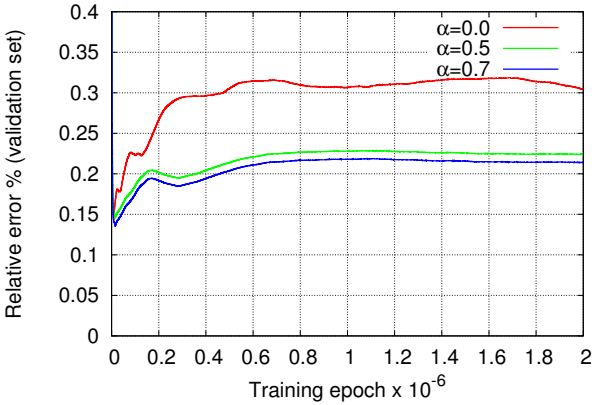

Figure 2.13: **Impact of momentum term on ANN generalization error**

combined among them. In this way the error of the resulting output value is reduced with respect to the one obtained from each network separately. This reduction is obtained in both fitting and generalization errors. The last one is the main goal of the hybridization, due to the difficulties to improve the generalization capability previously discussed.

In order to have a proper hybridization, the errors of the networks employed must have null average and to be mutually independently. It is reasonable to think that a similar condition can be satisfy employing networks very different among them. In practise this means to use a different weights initialization, structure of the network, e.g. different neuron number and activation function, learning and momentum coefficient. Moreover, each network can be trained with only a part of the available examples: the fitting set can be divide into "N" groups with only same example shared among the networks. The higher is the error independence, and better will be the hybridization effects. Three are the most used methods to combine the networks output:

- Naive method
- Basic Ensemble Method (B.E.M.)
- Generalized Ensemble Method (G.E.M.)

The first one is the most easy to apply but also the less efficient. In practise, once the "N" network were trained the user will choose to use the network with the lower error, losing all the knowledge stored by the other networks during the training.

In the second method (B.E.M.), the final output is obtained by averaging the outputs of the "N" networks trained (2.12), thus exploiting all the knowledge acquired by all the networks.

$$y(i) = \frac{1}{N} \sum_{i=1}^{N} y_i(j) \tag{2.12}$$

Defining:

$$m(i) = f(x) - f_i(x) \tag{2.13}$$

the deviation of the true function the rebuilding one, and:

$$MSE[f_i] = E[m_i^2] \tag{2.14}$$

the mean square error of each networks in term of m_i, it is possible to estimate that the average of the mean square errors is reduced of "N" times:

$$\overline{MSE} = \frac{1}{N}\sum_{i=1}^{N} E[m_i^2] \tag{2.15}$$

The G.E.M. method generalized the approach previously discussed. In this method the outputs of "N" networks are combined with a weighted average. In this way the networks which provide a higher error have a lower impact on the final output. This is computed modifying the equation (2.12) as follow:

$$y(i) = \frac{1}{N}\sum_{i=1}^{N} \alpha_i y_i(j) \tag{2.16}$$

Here α is the weight of network i, defined by:

$$\alpha_i = \frac{e_i^{-2}}{\sum_{j=1}^{N} e_j^{-2}} \quad \text{with} \quad \sum_{i=1}^{N} \alpha_i = 1 \tag{2.17}$$

where σ represent the error of network i. From a mathematical point of view, the error made with this third method will be always less or equal to the one made with the others two, since these are particular cases of the last one. An example of the improvement obtainable with a hybrid network is shown in Figure 2.14. The prediction of a single ANN is compared to the one of a hybrid network (ten ANN) in which the outputs were combined using the G.E.M. method. This results were compared to the output of the validation set employed for the selection of both learning and momentum coefficients:

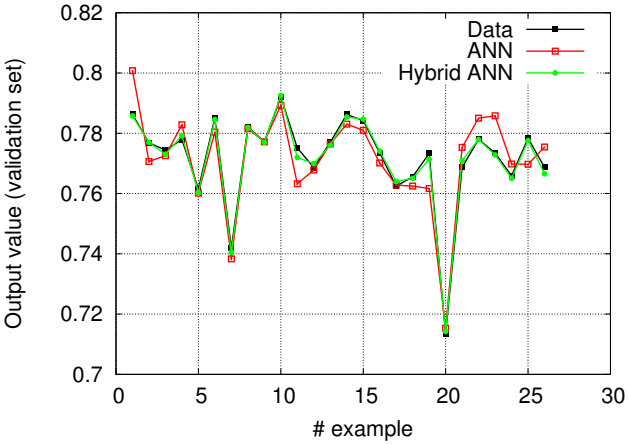

Figure 2.14: **Effect of network hybridization on ANN generalization**

for the sake of clarity only few data are reported without alter the content of the picture. The figure highlights the better generalization capability of the hybrid network, which rebuild with higher accuracy the trend of the value of the validation set. The drawback of use the hybrid ANN lies on the training time-consumption which will be "N" times the one of a single network. However, the use a cluster multi-cores to perform the learning phase drastically minimize this aspect.

Chapter 3

TRAF code

In this chapter the characteristics of the CFD code used for calculations will be described. Some more details concerning the model used to solve transitional flows, and the boundary conditions for surface roughness and shroud leakages computations will be reported.

3.1 The flow solver

In the present work, the multi-row, multi-block version of the TRAF solver was used (Arnone [29, 30]). The unsteady, three-dimensional, Reynolds averaged Navier-Stokes equations are written in conservative form in a curvilinear, body fitted coordinate system and solved for density, absolute momentum components, and total energy. The spatial discretization of the equations is based on a finite volume cell-centered scheme on non-periodic C-, H-, and O-type grids (Fig. 3.1). Both scalar and matrix dissipation models introduced by Jameson et al. [31] and Swanson and Turkel [32], together with an eigenvalue scaling, were implemented, to minimize the amount of artificial diffusion inside the shear layers. The system of governing equations is advanced in time using an ex-

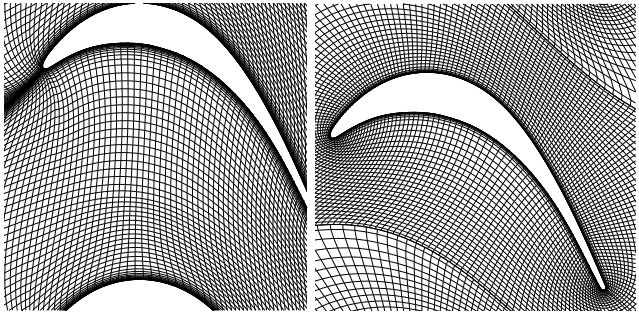

Figure 3.1: **Examples of non-periodic, viscous grids**

plicit four-stage Runge-Kutta scheme. Implicit residual smoothing, local time-stepping, multi-grid full-approximation storage (FAS) and grid refinement are employed in order to speed-up convergence to the steady state solution. The code features simple algebraic models and advanced multi-equation turbulence closures [33, 34, 35, 36].

3.1.1 Transition and turbulence modelling

The classical Wilcox's low-Reynolds number $k-\omega$ model [35], widely used in turbomachinery calculations, is applied in combination with the laminar kinetic energy model, which enables to take into account the pre-transitional rise of the fluctuating kinetic energy [37, 36](Fig. 3.2).

The laminar and turbulent kinetic energy equation can be written as follows:

$$\frac{Dk_\ell}{Dt} = P_\ell - 2\nu\frac{k_\ell}{y^2} + \nu\nabla^2 k_\ell - R \tag{3.1}$$

$$\frac{Dk}{Dt} = P_k - \beta^* k\omega + \frac{\partial}{\partial x_j}\left[(\nu + \sigma_k\nu_T)\,\frac{\partial k}{\partial x_j}\right] + R \tag{3.2}$$

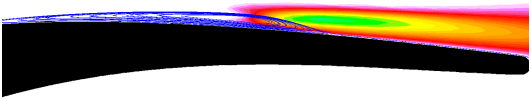

Figure 3.2: **Examples of total kinetic energy contours in a separated shear layer**

where $\beta^* = 0.09$, and

$$R = C_2(1 - e^{-\psi/C_3})\omega k_\ell \tag{3.3}$$

is a function used to transfer energy from k_ℓ to k, $\psi = \max(R_y - C_4, 0)$ is a transition parameter based on the wall-normal-distance Reynolds number R_y, $C_2 = 1.0$, $C_3 = 8$ and $C_4 = 10$. The production term of the laminar kinetic energy is $P_\ell = \nu_\ell S^2$, where S is the shear rate and ν_ℓ is the "laminar eddy-viscosity", which is modelled as follows:

$$\nu_\ell = C_1 \sqrt{k_\ell} \delta_\Omega \tag{3.4}$$

with $C_1 = 1$. For details on the implementation see Pacciani et al. [36, 38].

The inlet conditions for k and ω are obtained from the prescribed values of free-stream turbulence intensity $k_\infty = {}^3/_2 T u_\infty^2 u_\infty^2$, and turbulence length scale $\omega_\infty = k_\infty^{1/2}/\ell_{T\infty}$. The inlet condition for k_ℓ is as follows: $k_{\ell\infty} = k_\infty$ (see [37] for more details).

Surface roughness model

According to Wilcox [35, 39] at the wall $k_w = 0$ and the value of ω is modified in order to account for the effects of surface

roughness:

$$\omega_w = \frac{v^{*2}}{\nu_w} S_R \; ; \; S_R = \begin{cases} 4\lambda_R^2 & , k_s^+ \leq 5 \\ \lambda_R + \left(4\lambda_R^2 - \lambda_R\right) e^{(5-k_s^+)} & , k_s^+ > 5 \end{cases} \tag{3.5}$$

v^* is the friction velocity, $k_s^+ = k_s v^*/\nu$ is the roughness height in wall units, and $\lambda_R = 100/k_s^+$. The constant C_1 in the laminar kinetic energy model Eq. 3.4 was calibrated in order to sensitize the transition to the roughness height k_s^+:

$$C_1 = f_1(k_s^+) = \max\left\{0.8, 2\tanh\left[\left(k_s^+/18.13\right)^{2/3}\right]\right\} \tag{3.6}$$

3.1.2 Shroud leakage model

In shrouded turbines, the leakage flows play an important role in the overall turbine performance. The physics of these secondary flows and their interaction with the mainstream flow have been intensively investigated in recent years (Wallis et al. [40], Pfau et al. [41], Rosic et al.[42]). These studies show that these complex, three-dimensional and non-uniform flows affect the main flow path, modifying the blade loading and pressure distribution near the endwalls. They also change the incidence and enhance the secondary flows in the next blade row, with a consequent rise of the associated losses. As discussed by Rosic et al. [43], the need to account for the leakage flows in a three-dimensional multistage calculation has led to the development of shroud models with varying degrees of complexity and computational costs. These models range from a simple "black box" approach, where the leakage flow is modeled by extracting and re-injecting the flow at given positions upstream and downstream of the blade row with a specified angle, to three-dimensional, multi-block, unsteady simulations including the mainstream, the shroud cavities and the seal tooth regions.

In this work, a simple one-dimensional model of shroud cavity was used (Rubechini et al. [44],[16]). For a specific

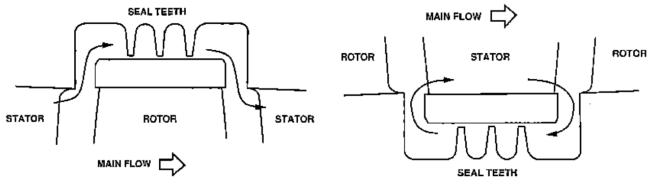

Figure 3.3: **Examples of shroud cavity**

shroud geometry (Fig. 3.3), the model calculates the leakage mass flow, total enthalpy rise and change in angular momentum through the cavity and the flow conditions at the interface between the cavity and the mainstream. Following an approach similar to that proposed by McGreeham and Ko [45], the flow through the shroud cavity is completely modeled, and its interaction with the main flow path is calculated by imposing coupled source/sink boundary conditions at the cavity/mainstream interface.

Chapter 4

Stage optimization

This chapter describes the optimization of a high-pressure stage for reaction steam turbine drums. Once discussed the redesign targets, the preliminary results obtained comparing the two meta-models previously described will be presented. Then the final optimum will be selected employing the SVM approach and its performance will be compared with the ones of the original geometry. Finally, a section will be devoted to the surface roughness related issue and its impact on blades design will be addressing.

4.1 Problem definition

The stage investigated is composed of prismatic blades and usually employed in both high and mid-pressure steam turbines. This type of blading is characterized by high aspect ratio (AR) and low radius ratio (RR). It is designed to work in a repeating stage environment and in a wide range of operating conditions, using a single airfoil geometry for stator and rotor rows.

The present optimization is aimed at maximizing the turbine's power output and efficiency, meeting the manufactura-

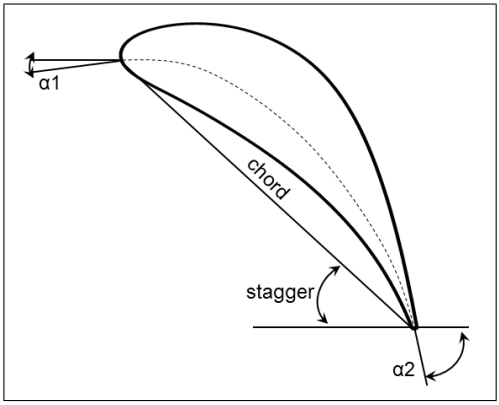

Figure 4.1: **Camber line optimization parameters**

bility constraints for the number of stages and the blade count of each stage. During the optimization process several constraints of a different nature were imposed in order to meet the present design rules. First of all, the mass flow rate was held constant. In this way the required stage loading increase was obtained without changing the operating point when replacing the original stage with the optimized one. Moreover, for the blade loading distribution over the airfoil surface and especially on the rear part of the suction side, limitation of the diffusion rate was imposed to avoid boundary layer separation. As far as the mechanical integrity issues are concerned, both the static and the dynamic behaviors of each geometry were checked downstream of the CFD analysis. Accounting for structural limitations is essential for final design purposes. It may guide the designer in choosing a given solution among several aerodynamic optima by eliminating those geometries that do not meet structural requirements. In the present optimization, the mechanical integrity checks relied on simplified design rules. They are based on the evaluation of root tensile stress and minimum inertia moment-to-area ratio (J_{min}/A),

ensuring the same mechanical capability for the optimized geometry as the original one.

In the first optimization step, a realistic geometry of the meridional flow-path was chosen, representative of an embedded stage of an existing HP/IP package. Bearing in mind that the optimized airfoil should operate in a wide range of flow coefficients, as the original one does, two different optimizations were carried out assuming boundary conditions representative of low and high flow coefficient operating conditions. To do this, two design points were identified, characterized by different mass flow rates and expansion ratios. Following this strategy, the whole range of operating conditions of interest will be covered by two optimized airfoils: the first working in the low-to-mid flow coefficient range, and the second working in the mid-to-high one.

A single airfoil for stator and rotor rows was used, according to the original design strategy. Such an assumption, together with that of prismatic blades, limited the parameters subjected to optimization to those of a single airfoil section, thus dramatically reducing the number of degrees of freedom of the redesign problem. As a consequence, the stage geometry was handled by varying only nine parameters in all, which control the camber line (Fig. 4.1) and thickness distribution over the airfoil for both stator and rotor rows simultaneously. The trailing edge thickness was maintained constant. The choice of which degrees of freedom employ, that is, which parameters modify during the redesign, was done by taking into account which of them had a relevant effect on the objective function considered. This is a crucial aspect if a good result from an optimization procedure would be obtained. In the author's experience the number of d.o.f. to adopt, must be that strictly necessary to allow the handling of the main parameters affected the objective functions of the redesign problem. In fact, when deals with the three-dimensional redesign of a turbomachinery component, the burst of the degrees of freedom is easy to achieve, with the consequence sudden increas-

ing of the design space's dimensions. Generally this occurs when the designer attempts to handle all the features of the geometry to optimize, making very hard for any optimization technique to really optimize all the parameters selected.

Once specified the range of variation of each parameters, the design space was populated using a quasi-random sampling. Then, the corresponding geometries were calculated by means of three-dimensional viscous run, employing the Wilcox's two-equations k-ω high-Reynolds model for the turbulence closure. In order to account for the repeating environment experienced by the stage within the actual turbine, suitable repeating boundary conditions were adopted, aimed at obtaining prescribed pressure and temperature drops while ensuring the same span-wise profiles at stage inlet and outlet (Rubechini et al. [16]). The training database generated was compound of about 2000 geometries: about 1800 for the fitting set and 200 for the validation one. It is worth noticing that, despite the high number of calculations and the low number of d.o.f., the design space is only well sampling and not fill fully populated. This make necessary the use of a tool that is able to rebuild the shape of the response surface with the better approximation possible.

In the successive sections, the results of the optimizations will be presented and discussed, in terms of performance curves over a wide range of operating conditions and comparison with the experimental measurements.

4.2 Experimental facility

The experimental investigation was performed in the blow-down facility for linear cascades located at the LFM (Laboratorio di Fluidodinamica delle Macchine) in Milan. This is a transonic wind tunnel with a test section of 80x470 mm, fed by 6000 kg of pressurized air stocked at 20 MPa (Dossena et al. [46, 47]), as depicted in Fig 4.2. For the purpose of the present work, cascade was composed of 9 blades and the cen-

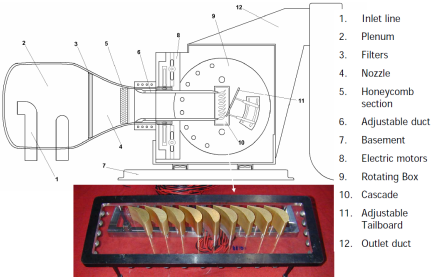

Figure 4.2: **Experimental test section scheme**

Table 4.1: **Cascade experimental conditions**

Total pressure	1 to 1.3 bar
Total temperature	288 K
Isentropic exit Mach	0.25 to 0.64
Reynolds	$3.5\text{x}10^5$ to $9.5\text{x}10^5$
Inlet flow angle	-20 to +30 degrees
Turb. intensity	$\simeq 1\%$

tral passage was outfitted with 36 pressure taps of 0.4 mm diameter, 20 located on the suction side and 16 on the pressure side. Flow field measurements were performed by traversing a miniaturized five hole probe with a head diameter of 1.8 mm on a plane located 0.5 axial chords downstream trailing edge: the measurement plane is defined by a grid of 50 points repeated -approximately every 2 mm equally spaced along two blade pitches- 10 times at different span-wise positions on one half of the blade height. The probe was calibrated in the range $\pm$ 25 deg and $\pm$ 16 deg in yaw and pitch angles respectively, and for Mach numbers ranging from 0.2 to 1.0. The estimated probe accuracy for static and total pressure is $\pm$ 0.3% of the dynamic pressure, while for flow angle mea-

surement is ± 0.2 degrees. A prismatic 3 hole probe was used for a continuous monitoring of inlet total pressure. In order to provide proper CFD inlet boundary conditions, a miniaturized flattened total pressure probe was traversed in the upstream boundary layer for all considered flow conditions. The inlet free-stream turbulence intensity was estimated 1% by means of hot wire anemometer measurements. The geometry of the airfoils were scaled up in order to obtain the best compromise between Reynolds number (based on chord and exit velocity) and cascade aspect ratio (about $AR = 1.4$). The experimental results are available in terms of surface loading distributions and enthalpy loss coefficients, defined by:

$$\zeta = 1 - \left(\frac{c_2}{c_{2is}}\right)^2$$

The aerodynamic measurements were performed at three different expansion ratios (PR), for Mach numbers ranging from 0.25 to 0.64. Due to the test rig layout, Reynolds and Mach numbers cannot be controlled independently, so the corresponding Reynolds numbers range from 3.5x10^5 to 9.5x10^5. For each pressure ratio, three different incidence angles were also tested in the broad range from −30 to +20 degrees. A summarized of the experimental conditions is reported in table 4.1.

4.3 Comparison between SVM and ANN approach

The first of the two optimization campaigns, the one at low flow coefficient, was performed employing both the metamodel described in chapter 2.

The results obtained with the support vector machine approach were compared with those of an hybrid artificial neural network. Both the models were trained using the same database, and their training parameters were selected in order

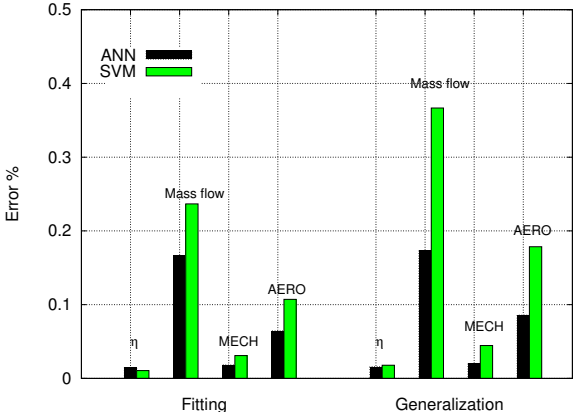

Figure 4.3: **Comparison between fitting and generalization errors for ANN and SVM**

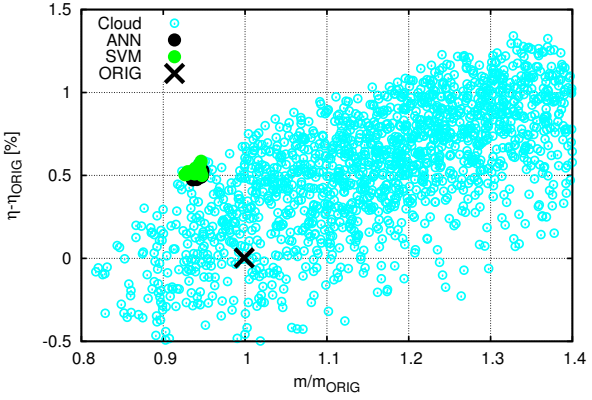

Figure 4.4: **Comparison between ANN and LS-SVM prediction capability: design space**

to get the best prediction accuracy. According to the parametric analyses reported in chapter 2, a value of $\gamma = 5.0\text{x}10^3$ and $\sigma = 0.1$ were chosen for the SVM training, while a value of $\eta = 0.5$ and $\alpha = 0.7$ were selected for the ten ANNs ones. A first important difference, between these two models, can be found in the number of training parameters to set up at the beginning. In particular, the ANN has got all the unknown referred to neurons and hidden layers number, which LS-SVM has not. Another consideration concerns the time consumption of the meta-model training: LS-SVM results lower expensive than ANN about two order of magnitude. This is a remarkable advantage mainly when deals with greater database and more degrees of freedom, because computing requirements assume a relevant importance compared to the overall procedure time.

Now, looking at the results. Concerning fitting and generalization errors (in percentage), figure 4.3 reports a first comparison between ANN and LS-SVM (MECH and AERO are referred to the static and dynamic constraints respectively). For both meta-models the errors are very low ($<$ 0.5%) and comparable for each objective function/constraint, with a narrow margin of advantage for ANN. This suggests that both tools were correctly trained and the number of samples used for the training was suitable. Once verified the learning of the meta-models, they were used to find a set of optimum solution and the suggested geometries were verified using CFD calculations (fig. 4.4). For both models, the suggested geometries lie on the Pareto front of the space investigated, and respect the imposed constraints for mass flow, diffusion rate and mechanical integrity check. In order to analyse the meta-models performance, the generalization error and the difference between models prediction and CFD computations is shown in figure 4.5. For each objective function, the generalization error obtained during the training is comparable to the one outcome, with a general better result for LS-SVM, confirming the training goods. These results high-

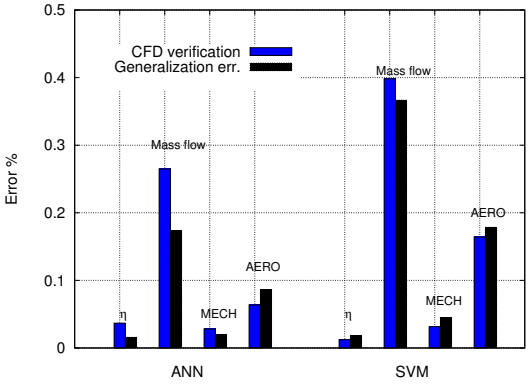

Figure 4.5: **Comparison between generalization error and CFD verification**

light the prediction capability of the LS-SVM, that seems more precise and consistent in terms of prevision ability than ANN, even if a critical review of the results, point out that the difference are not so big. Figure 4.6 and 4.7 shows a comparison between meta-models prediction and CFD verification. According to the errors show in figure 4.5 the prediction is very good for all the objective functions, and the two models demonstrate to well understood the effect that each parameters have on the optimization targets. In particular, LS-SVM have a better accuracy than ANN concerning the efficiency prevision (fig. 4.6), even if the difference is small (about 0.05%) in this case also. An explanation can be given analyzing figure 4.8 and 4.9, where the efficiency trend with respect to two of the nine parameters subjected to optimization is shown. The two meta-models approximate the design space with high accuracy, but in different way. From the results seems that the LS-SVM have learned with a better accuracy the impact on efficiency of these two parameters, while respecting the imposed constraints.

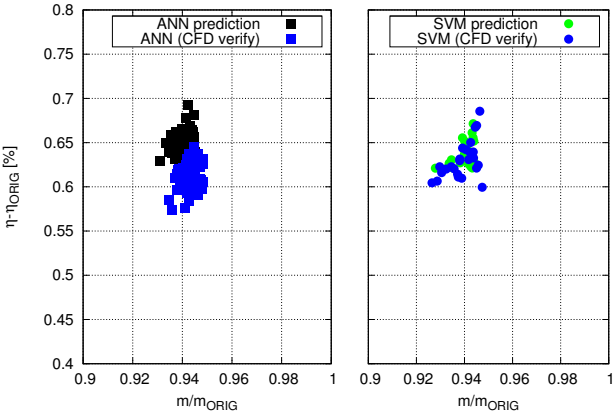

Figure 4.6: **Comparison between ANN and LS-SVM prediction capability: efficiency and mass flow rate**

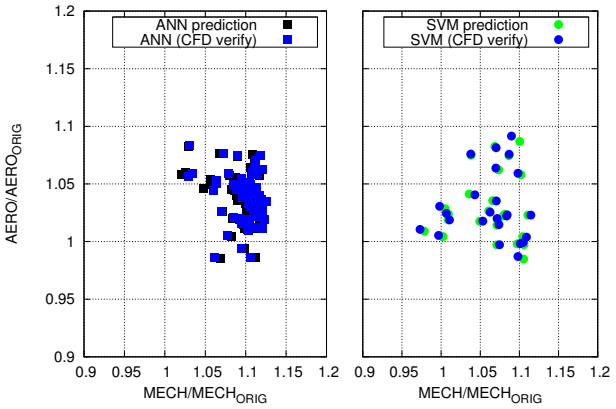

Figure 4.7: **Comparison between ANN and LS-SVM prediction capability: MECH (static) and AERO (dynamic) constraints**

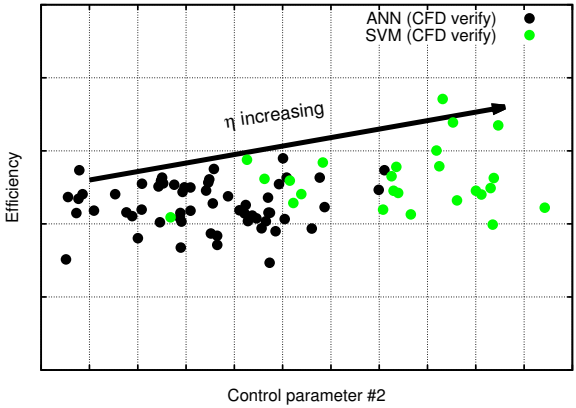

Figure 4.8: **Efficiency trend with respect to control parameters #2**

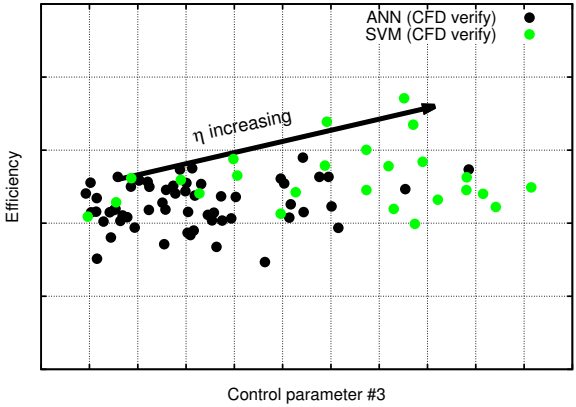

Figure 4.9: **Efficiency trend with respect to control parameters #3**

For all these reasons, the second optimization campaign and the choice of the final optimums were carried out employing the SVM.

4.4 Optimization results

Two different optimizations, performed at both high and low flow coefficient conditions, were carried out to achieve the optimization targets. As a result, two different optimum airfoils were identified. Each one of these airfoils, hereafter referred to as OPT-A (for low ϕ) and OPT-B (for high ϕ) respectively, were tested in off-design conditions by varying the stage pressure drop. The goal was to draw a performance curve in the range of interest, thus providing two optimum curves at low and high flow coefficient conditions. Two equivalent curves were obtained by setting the original airfoil at two different stagger angles, in order to cover the same flow coefficient range. In addition, both optimized airfoils were re-staggered to cover the whole operating range: the OPT-A one was opened and tested at high flow coefficient, whereas the OPT-B one was closed to fit the low ϕ region.

Fig. 4.10 shows the comparison between the efficiency curves of the original airfoil and those of the optimized airfoils. The efficiency gain obtained from the optimizations, in terms of peak-to-peak $\Delta\eta$ from original geometry, is about 0.5% for the OPT-A airfoil (low ϕ), and 1.25% for the OPT-B one (high ϕ). The new geometries exhibit similar operating range as the original, and maintain an elevated efficiency gain in off-design conditions. It is worth noting that the position of the peak efficiency undergoes a shift towards the low flow coefficients for the optimized geometries. This is due to a different position of the new airfoils in the $\phi - \psi$ chart, as shown in Fig. 4.11, associated with the blade loading increase required as optimization target.

Fig. 4.10 also shows how similar the OPT-A performance is to the re-staggered version of the OPT-B, closed to fit the

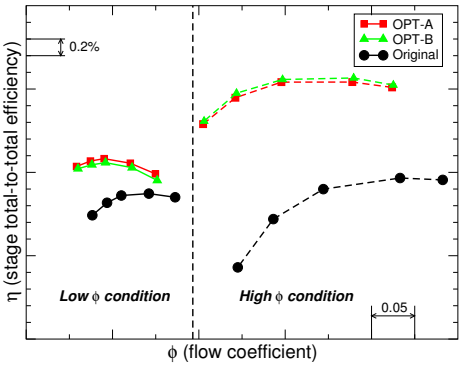

Figure 4.10: **Efficiency comparison: original and optimized geometries performance curve (CFD)**

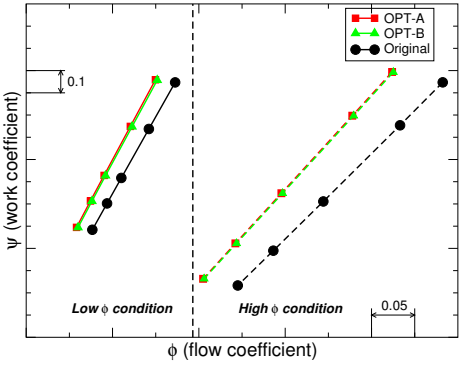

Figure 4.11: **Work coefficient comparison: original and optimized geometries performance curve (CFD)**

same $\phi - \psi$ working line, and the same holds true when comparing the OPT-B geometry to the opened version on the OPT-A one. In both cases, the benefits of using the native

optimized airfoil instead of the re-staggered one seem quite small, with a peak-to-peak $\Delta\eta$ of about 0.03%. This important result, due to the fact that mechanical constraints were independent of the operating conditions and thus driving the two optimizations towards similar airfoil shapes with different stagger angles, suggested the possibility of using a single optimized airfoil: besides a negligible lack in performance, the overall design process greatly benefits from the ease of managing a single airfoil. In light of these considerations, and observing that most of the existing stages are actually designed to work at low flow coefficients, the OPT-A was selected to cover, by re-staggering, the entire operating range. A complete characterization of such an airfoil (which hereafter will be referred to as the OPT airfoil) will be presented in chapter 5.

Compared to the original design, the OPT geometry is thinner, has a higher nominal stagger angle (by about 8 degrees) and a smaller radius of curvature in the rear part of the suction side (Fig. 4.12). The large leading edge exhibited

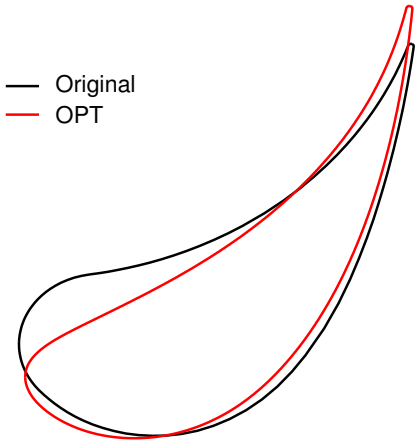

Figure 4.12: **Airfoil geometries comparison**

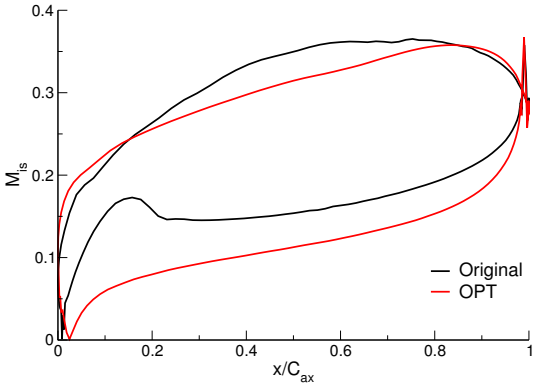

Figure 4.13: **Isentropic Mach number distribution: comparison between original and OPT (CFD)**

by both airfoils ensures a good mechanical capability and robustness with respect to incidence required for the wide operating range whereby these blades are thought. The reduction of thickness, limited by structural constraints, has played an important role in increasing the efficiency, in fact the optimization pushed towards the reduction of the thickness-to-chord ratio. The combination of the other two new features, higher stagger and smaller radius of curvature, has provided the loading increase. Moreover, the small radius of curvature leads to move the blade loading towards the uncovered part of the suction surface, thus producing a more aft-loaded distribution (Fig. 4.13) and an increase of the diffusion rate (about 10%). A comparison in terms of isentropic Mach distribution is shown in Fig. 4.13, where it can be observed the most uniform distribution of the OPT airfoil. It is the detailed control of the pressure and suction surfaces curvature, and the asymmetric thickness distribution in the leading edge region, that produced a smooth acceleration on the pressure side.

Parallel to the numerical activity, an experimental cam-

paign was conducted in which both the original and the OPT airfoils were tested in the linear cascade arrangement described in section 4.2.

Although the experimental campaign was mainly focused on the characterization of the mid-span airfoil section, the measurements were performed at ten spanwise positions, over one half of the blade height. This allowed the comparison between measurements and CFD not only in terms of 2D results at mid-span (profile losses, velocity distributions), but also in terms of spanwise distributions of flow angle and loss coefficient. To do this, CFD calculations were carried out over the 3D cascade geometry, by imposing the measured boundary conditions (inlet profiles, outlet static pressure profile) in order to reproduce as accurately as possible the experimental operating conditions. According the low turbulence intensity and to relatively low Reynolds numbers, transitional conditions are likely to be found within the test rig. For this reason, calculations were performed using a low-Reynolds formulation of the two-equation k-ω model.

The results of such computations, in terms of spanwise distributions of loss coefficient and blade-to-blade exit flow angle, are shown in Figures 4.14 and 4.15. The comparison is quite encouraging, showing a substantial agreement between the test rig environment and the computational one. Such a good agreement is confirmed by looking at the surface pressure distributions at mid-span, reported in Figures 4.16 and 4.17 for both the original and the optimized geometries.

The main goal of the experimental activity was to confirm the performance increase of the new OPT airfoil over the original one in terms of profile loss. Figures 4.18 to 4.20 report the predicted and measured lapse rates, at cascade midspan, for three different incidence angles at varying Mach numbers from 0.25 to 0.64 (and Reynolds numbers from $3.5\text{x}10^5$ to $9.5\text{x}10^5$).

As a first comment, it can be noticed that the measurements confirm, for any pressure ratio and incidence angle,

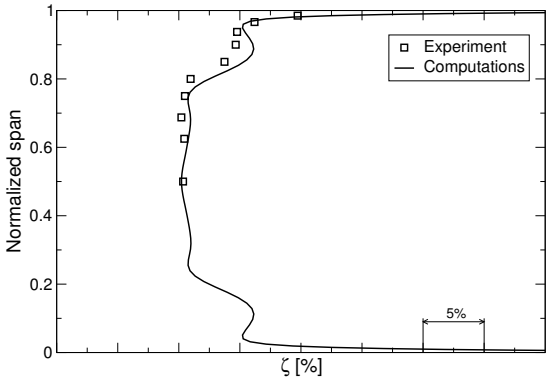

Figure 4.14: **Experimental and computational enthalpy loss coefficient span distribution: original airfoil,** $M_{is} = 0.47$ **and zero incidence case**

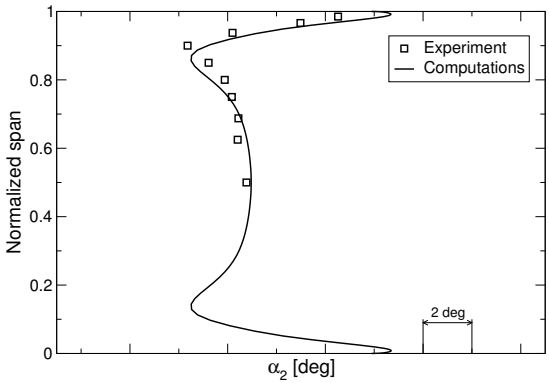

Figure 4.15: **Experimental and computational blade-to-blade exit angle span distribution: original airfoil,** $M_{is} = 0.47$ **and zero incidence case**

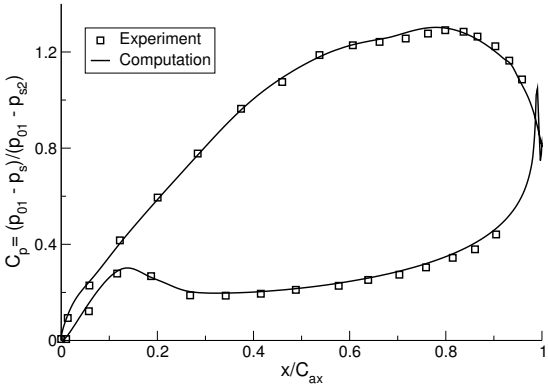

Figure 4.16: **Experimental and computational pressure coefficient distribution: original airfoil, zero incidence case**

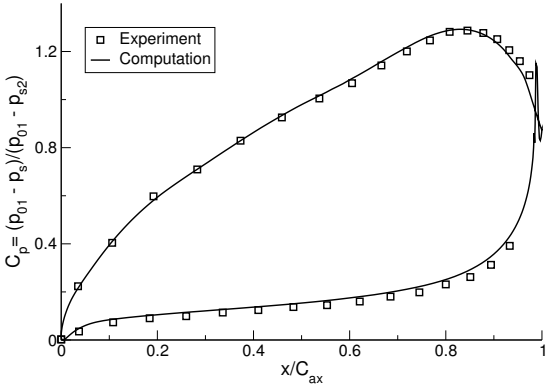

Figure 4.17: **Experimental and computational pressure coefficient distribution: optimized airfoil, zero incidence case**

the superiority of the OPT airfoil. A general agreement is observed between measures and predictions in terms of shape of the loss curves, which follow the theoretical trend of loss reduction with increasing Reynolds number. Moreover, the loss level is also fairly well predicted, the maximum error between computations and measurements being lower than 0.3%.

More specifically, some appreciable differences arise for the highest Mach (and hence Reynolds) number cases, especially at off-design incidences. At any incidence, computations predict the same loss-decreasing trend for both the original and the OPT airfoils, whereas measurements highlight a different tendency between the two airfoils. In particular, for the OPT airfoil, at $M_2 = 0.64$ the measured profile loss remains almost constant for the -30 negative incidence case, and slightly rises for the $+20$ positive one. This behavior, which is limited to the highest Reynolds, off-design incidence cases, is likely to be related to transitional issues: the OPT airfoil might undergo an earlier transition, thus increasing the profile loss with respect to the CFD-predicted value. It should be remarked that, although calculations where carried out using a transition-sensitive turbulence model, many factors could prevent from completely reproducing the transitional behavior within the actual cascade for all investigated configurations. Just to cite a few among these factors, we may address the inherent sensitivity of CFD-predicted transitional behavior to the turbulence modeling, the uncertainty affecting inlet turbulence characteristics (intensity, length scale), and the impact of the actual surface roughness on transition onset.

Whatever the reason of the small discrepancy between predictions and measurements for the highest Reynolds numbers, measurements confirm in all cases the superiority of the OPT airfoil over the original one. Furthermore, considering that in a real machine these airfoils deal with higher Reynolds numbers and turbulence intensities, and that the benefits of the OPT airfoil increase the closer they get fully-

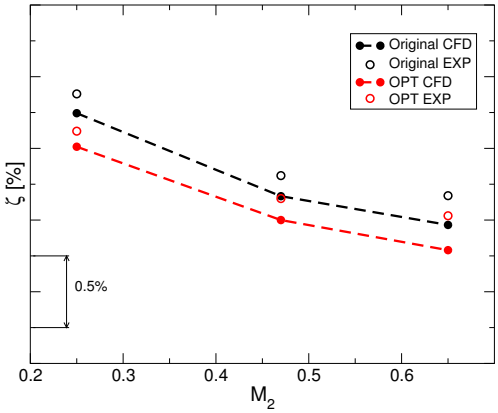

Figure 4.18: **Experimental and numerical enthalpy loss coefficient: midspan values, zero incidence case**

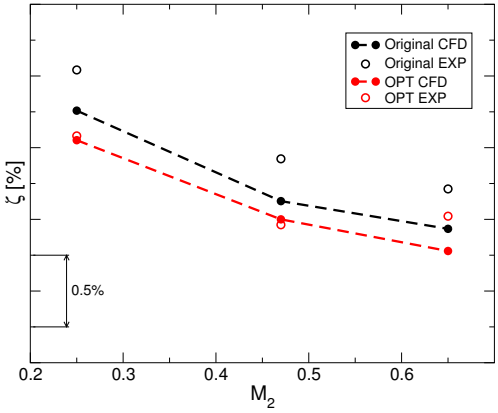

Figure 4.19: **Experimental and numerical enthalpy loss coefficient: midspan values, incidence +20 degrees case**

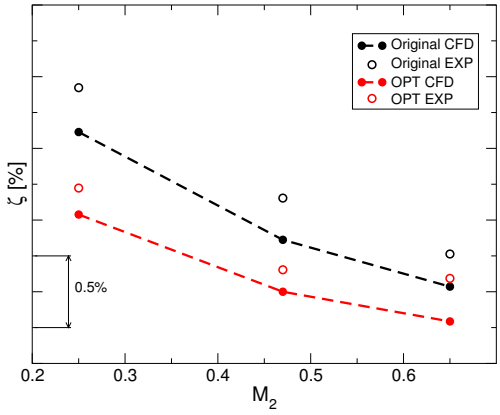

Figure 4.20: **Experimental and numerical enthalpy loss coefficient: midspan values, incidence -30 degrees case**

turbulent conditions, even greater benefits would be reasonably expected in real turbine applications.

4.5 Impact of surface roughness

In all the calculations performed during the optimization campaigns, the wall boundary condition was set according to the formulation for hydraulically smooth surface. Thus a verification of the impact of roughness on the stage performance is mandatory for addressing the design of new stage. The results will be presented for the optimized geometry only and in a non-dimensional format, in order to have a general character and to be extended to the original geometry also.

4.5.1 Background information

The effects related to the blade surface roughness are a well-known issue for the turbomachinery designer, in particular

when dealing with the estimation of the components' performance.

The influence of surface finishing on the behavior of the adjacent flow is an aspect studied by researchers for nearly a century. The basis of these studies are the works of Nikuradse [48] and Schlichting [49], which approached the roughness related issue in rough pipes and flat plates. On the base of these pioneering works, many researchers have continued to study both experimentally and numerically the effects of surface roughness on the turbomachineries performance. A vast amount of literature on the subject is available to the turbomachinery community, likely due to the many aspects that are involved with it (Bons [50], Flack and Schultz [51]). Once the equivalent sand grain methodology proposed by Schlichting [52] was accepted, from an experimental point of view, many efforts were made to characterize surface finishing. The goal was to find an empirical correlation to convert the metrics roughness (R_a, R_t and so on) into a sand grain (k_s) one, and to employ this parameter for comparison purposes and to fine tune closure models of numerical codes. Much progress was made in this direction, but unfortunately, because of the huge variety of surface typologies (nowadays also analysed by three-dimensional techniques), there is no unique correlation which solves this issue. It is worthwhile noticing that the conversion factor to obtain the sand grain roughness parameter can vary up to a factor of five, depending on the correlation adopted (Bons [50]). Some criteria employ the standard metrics roughness such as the one proposed by Speidel [53] and Hummel et al. [54]. Other authors have tried to characterize the shape of the rough element, and to extract a roughness density parameter to use in their correlation. Among these, the ones proposed by Dirling [55], Sigal and Danberg [56], van Rij et al. [57], and Waigh and Kind [58] are some of the most often used.

Many other works concerned with experimental tests were performed in cascade rigs as well as in multi-stage environ-

ments. The goal was to provide detailed information on the effects that roughness has on the components' performance. Zhang et. al [59] studied the influence of surface roughness on the aerodynamic losses of a turbine vane, analysing the effects of different rough surfaces (uniform and variable) and Mach number distributions. They found a loss increase with the increase of the exit Mach number, and quantitative and qualitative different flow characteristics by varying roughness. Im et al. [60] investigated the effect of leading edge roughness and Reynolds number on compressor profile loss. They found a high impact of rough blade on performance even if only 2% of the blade pressure and suction side was rugged. This was mainly due to the influence of the rough surface on the suction side laminar separation bubble: the losses were reduced at lower Reynolds numbers and increased at the higher ones. Vázquez and Torre [61], and Hodson and Howell [62] studied the effect of surface roughness on efficiency of a low pressure turbine. Their results suggested that at high altitude, the effect of "as-cast"rough airfoils did not affect the efficiency.

The research has been active from the numerical point of view too. Many efforts were made to take into account the roughness with an appropriate wall boundary condition for the turbulence closure. In the work of Boyle [63], a numerical investigation of the effects of incidence and surface roughness was carried out, using the roughness model proposed by Cebeci and Chang. The performance of a two-stage turbine over a wide range of operating conditions was computed. A good agreement was found between computations and measurements in terms of turbine efficiency for both the smooth and the rough blades. A numerical and experimental investigation of the effects of roughness in compressor blades was carried out by Mesbah et al. [64]. They compared the results obtained with three different turbulence models, $k-L$, $k-\omega$ and Spalart-Allmaras, with the measurements in terms of blade load distributions and losses. A good agreement was only found for the smooth blade. Boyle and Senyitko [65]

reported an experimental and numerical analysis of surface roughness effects on a turbine vane, for four exit Mach numbers and three turbulence intensities. In their work, several metrics-to-sand grain roughness correlations were compared. Moreover, a comparison between the results obtained with the Cebeci and Chang [66], and the Wilcox roughness models were presented. Good results were obtained using the Cebeci model coupled with Mayle's [67] transition model, compared to the poor predictions obtained with Wilcox's model.

4.5.2 Experimental measurements

Test rig

The experimental investigation was carried out in the blow-down facility for linear cascades located at the LFM (Laboratorio di Fluidodinamica delle Macchine) at Politecnico di Milano. This is a transonic wind tunnel with a test section of 80 mm height and 470 mm wide, fed by 6000 kg of pressurized air stocked at 200 bar. For the aim of the present research, the cascade was composed of 9 blades (Fig. 4.2). Several repetitions (5 to 10) of the same test were performed to have a wider statistic analysis and reduce measurement uncertainty. The periodicity condition was achieved by means of a movable tailboard located downstream of the cascade: the differences in flow field measured downstream of the central passages were found to be within the measurements accuracy. The blade geometry represents a typical stator employed in reaction stages of high/intermediate pressure steam turbines. The blades were scaled up, in order to obtain the best compromise between Reynolds number range (based on chord and exit velocity) and cascade aspect ratio (about $AR = 1.3$). The Reynolds number variation was obtained by pressurizing the test section in the range from 1 to 3.5 bar, by means of a variable sonic throat located at the outlet section of the wind tunnel. To guarantee an independent fine tuning of both Reynolds and Mach numbers, an 8" butterfly valve

Table 4.2: **Cascade experimental conditions**

Total pressure	1 to 3.5 bar
Total temperature	250 to 295 K
Isentropic exit Mach	0.50
Reynolds	$0.7\text{x}10^6$ to $2.5\text{x}10^6$
Turb. intensity	$\simeq 1\%$

Table 4.3: **Cascade data**

Aspect ratio	1.3
Flow deflection	73^o
Zweifeil number	0.70

and a 2" regulation valve were installed. The whole range of Reynolds numbers from $0.7\text{x}10^6$ to $2.5\text{x}10^6$ - characteristic of typical steam turbines blades of different sizes -, was covered by means of 10 to 20 points for each surface roughness considered. Data reported here have been collected at the same expansion ratio - i.e. at a downstream isentropic Mach number of approximately 0.5 -, irrespective of the Reynolds number. The cascade inlet flow angle was set in order to have nominal incidence on the blade. A summary of experimental conditions and cascade data are reported in Tables 4.2 and 4.3.

Detailed measurements of the 3D flow field downstream of the cascade have been performed by traversing at midspan a miniaturized five-hole probe (head 1.8 mm) at a distance of 50% of the blade axial chord. The five-hole probe measurement grid was defined by 50 points spaced equally (approximately 1mm) along a single blade passage. The five-hole probe was pre-aligned to the downstream pitch-wise mass averaged flow angle evaluated at atmospheric back pressure condition. The central hole of the downstream probe was con-

Table 4.4: **Shot-peening micro-spheres features**

k_s/C	Diameter [mm]	Material
$0.4\text{x}10^{-4}$	0.21-0.3	Ceramic
$0.8\text{x}10^{-4}$	0.21-0.3	Ceramic
$0.9\text{x}10^{-4}$	0.21-0.3	Ceramic
$1.6\text{x}10^{-4}$	0.4	Steel
$2.5\text{x}10^{-4}$	0.4	Steel

nected to a very high accuracy differential pressure transducer. It was directly coupled on the reference side to the upstream total pressure line supplied by a three-hole probe located one axial chord upstream of the cascade. Since the maximum local flow angle variation downstream of the blades in all the tests with respect to the probe pre-alignment was 1 degree, the total pressure coefficient of the five-hole probe was always null (i.e. the correction to be applied on the pressure reading of the central hole to obtain the local flow total pressure is null). This means that the central hole pressure reading was coincident with the local actual total pressure of the flow. In this operating conditions, the uncertainty of the local total pressure drop measurement is dramatically reduced, since only the differential pressure transducer uncertainty is involved in the measurement chain, thus excluding the uncertainty involved in the whole probe calibration process.

The surface roughness variation was obtained by a progressive machining of the blades, by means of shot-peening using micro-spheres of different diameter. Thus, five roughness values ranging from k_s/C=$0.4\text{x}10^{-4}$ to $2.5\text{x}10^{-4}$ were considered in the frame of the present work. The smallest of them can be considered equivalent to the finish of a smooth blade. The conversion factor between metrics R_t and equivalent sand grain roughness k_s was defined as suggested by

Speidel [53] and Schlichting [49], and defined by:

$$k_s = \frac{R_t}{2.56} \tag{4.1}$$

More details about roughness and the shot-peening procedure are reported in Table 4.4.

Finally, in order to complete the data set required for CFD computations, total temperature, flow angle and turbulence intensity (estimated $Tu \simeq 1\%$) at the cascade inlet were also measured.

Results

The experimental results were available in terms of blade loading and mass averaged total pressure loss coefficient Y, defined by:

$$Y = \frac{p_{01} - p_{02}}{p_{02} - p_{s2}} \tag{4.2}$$

The campaign was mainly focused on the investigation of the surface roughness effects on the profile losses, thus the measurements were performed at cascade midspan. The blade loading was measured for the smooth blade only, that is before shot-peening.

Experimental results are summarized in Fig. 4.21, where the loss coefficient is reported as a function of the Reynolds number for all the k_s/C investigated. In this plot, as well as for the other successive plots, losses are normalized with respect to the value at $Re_2 = 1x10^6$ and $k_s/C = 1.6x10^{-4}$. The shape of the curve for lower k_s/C, suggests that the campaign was carried out in a range of Reynolds number for which the boundary layer over the blade surface is laminar for a large part of the suction side. In fact, the trend is very close to the $Re^{-0.5}$ curve that represents the loss trend of a laminar boundary layer.

Looking at the other curves, increasing the surface roughness leads to a shift of the critical Reynolds ($Re_{2,cr}$) towards smaller values. Here $Re_{2,cr}$ is defined as the value at which

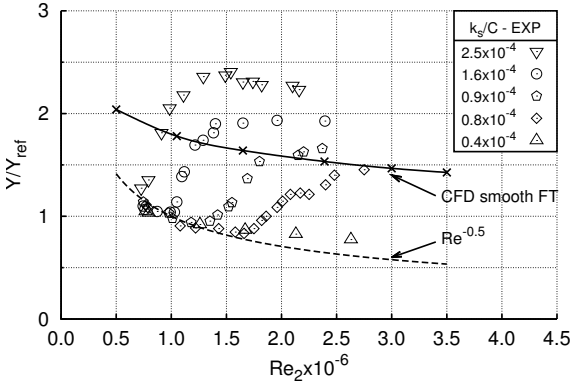

Figure 4.21: **Experimental total pressure loss coefficient**

the loss curves start to differ from the laminar trend. The sudden increase in the profile loss is due to boundary layer laminar-to-turbulent transition, and the shape of this increase depends on the combined effect of $Re_{2,cr}$ and k_s/C: lower roughnesses lead to a mild increase and vice-versa. This scenario suggests that most of the data lie in a region where the boundary layer is mainly transitional. For the higher roughness only, the fully-rough regime is reached for the higher Reynolds number measured. These considerations are similar to the results found by Boyle and Senyitko [65] in their cascade test rig by varying surface roughness. In their study, wide regions of laminar flow were also found in particular for the smooth blade case. Moreover, these results are in line with the statement of Bons[50], whereby in a clean/quiet wind tunnel it is possible to obtain a transition Reynolds number of about $3x10^6$.

Similar considerations on the transitional nature of these experiments can be inferred from Fig. 4.22 and 4.23. Profile losses are shown as a function of k_s/C in Fig. 4.22 and Re_{2,k_s} in Fig. 4.23 respectively. In both plots, each curve is

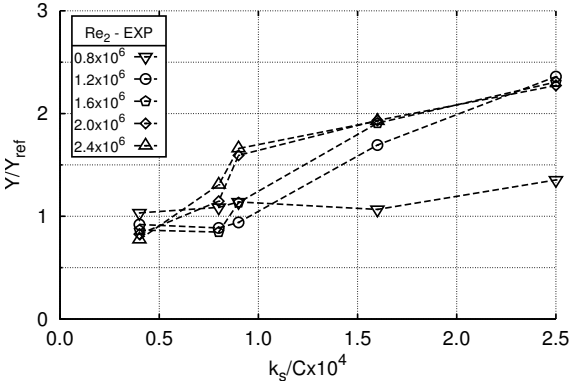

Figure 4.22: **Experimental total pressure loss coefficient for several Reynolds number tested**

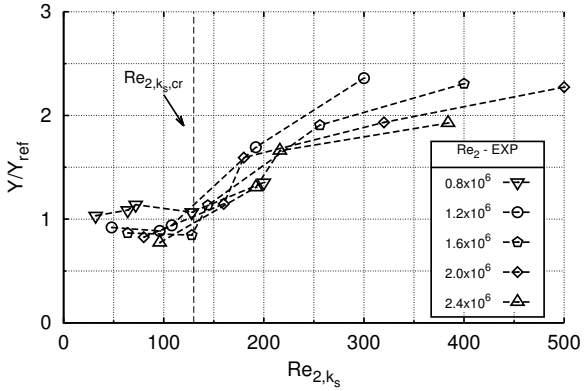

Figure 4.23: **Experimental total pressure loss coefficient for several Reynolds number tested**

associated with a different Reynolds number value: for the sake of clarity only the most significant Reynolds numbers are reported. In Fig. 4.22, the plot shows a region of low and quite constant losses for the lower roughness (laminar boundary layer). A steep increase in the loss coefficient is found when both k_s/C and Re_2 are increased, corresponding to the trigger of boundary layer transition. Then, a substantial loss independence from the Reynolds number is observed. These trends are similar to the ones found by Speidel [68] by means of an experimental campaign carried out in a linear cascade, and re-discussed by Schlichting [52]. In that case, the discussion was mainly focused on the impact of blade pressure distribution on boundary layer transition for different roughness values. As found in the present work, the results pointed out wide regions of laminar flow over the blade in cascade conditions. Figure 4.23 allows an estimation of $Re_{2,k_s,cr}$ whereby the transition is induced by roughness of about 130. This value is in good agreement with the one proposed by Feindt [69], and suggests that the conversion factor from R_t to k_s of 2.56 used, is reasonable for the present case.

4.5.3 Numerical results

Cascade environment

The experimental data obtained for the cascade were used to fine tune the roughness model. The goal of the calibration was to improve the model's capability of predicting roughness-transitional flows. Then, the tuned model will be used to predict the impact of roughness in an actual stage environment.

Three-dimensional viscous steady runs were performed in order to match the experimental measurements. A 340x64x72 O-type grid (Fig. 4.24) with a $y^+ \simeq 0.1$ was used to ensure high accuracy and reliability of the computations.

A first comparison between experiments and computations concern the blade loading. Figure 4.25 shows a substan-

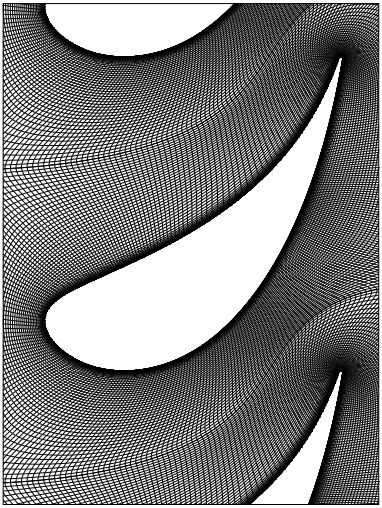

Figure 4.24: **Cascade two-dimensional O-type grid**

tial agreement between the test rig environment and computational one.

The model calibration was started from the measurements at $k_s/C = 1.6\text{x}10^{-4}$, for which laminar, transitional, and fully-rough flow regimes are successively encountered at increasing exit Reynolds numbers. A parametric study was carried out in order to calibrate the numerical transition by varying the model constant $C1$ (see Eq. (3.4)). This parameter controls the laminar kinetic energy production, playing a role of crucial importance in determining the $Re_{2,cr}$ that triggers the transition, and the consequent loss increasing. The analysis led to the correlation reported in Eq. (3.6). Such a tuning was extended to all the tested surface roughness, and the results are summarized in Fig. 4.26. The comparison shows a generally good agreement, in particular the Re_{cr} and the subsequent increasing of losses are well predicted.

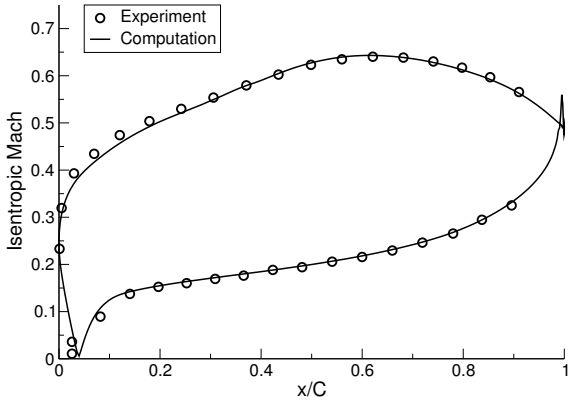

Figure 4.25: **Smooth blade experimental and computational isentropic Mach distribution**

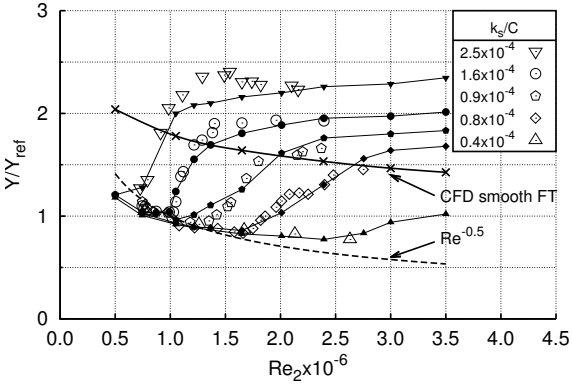

Figure 4.26: **Total pressure loss coefficient: experimental (open symbol) and CFD (filled symbol and solid line) results**

The computations confirm wide region of laminar flow for $Re_2 < Re_{2,cr}$. For higher values, the boundary layer undergoes the laminar-to-turbulent transition and the extension of the turbulent portion grows with the Reynolds number. Thus, a quasi fully-rough regime can be considered to be reached at higher Re_2, in particular for the higher values of k_s.

From the analysis of Fig. 4.26, two considerations can be made. The first one concerns the transitional flow region. Fixing the value of the Reynolds number, the increase of losses while increasing k_s/C depends on two phenomena which act at the same time: the first concerns the augmentation in losses due to the rough surface, while the second one is linked to the boundary layer transition. The combination of these two aspects yields a sudden increase in the profile loss, up to 1.5-2 time the value depending on the case. The second consideration instead concerns the turbulent region. The effect of transition on losses is negligible and only the roughness variation is accountable for loss increases. That is, this augmentation has to be comparable to the one estimated in a fully-rough regime. CFD results predict a ratio between the loss coefficient Y (at highest Re_2 and k_s/C) and the one for the smooth surface in fully-turbulent condition Y_{smooth} of about 1.58. This result is in very good agreement with the value of $Y/Y_{smooth} \simeq 1.55$ obtained with the correlation of Craig & Cox [70], which is widely used for turbomachinery applications. Similar results are found by using the correlations proposed by Aungier [71].

Real stage environment

The proposed numerical framework was successively used to carry out a comprehensive CFD analysis of a high-pressure steam turbine stage. The goal was to investigate the influence of roughness on the losses over the whole stage envelope.

With respect to the cascade measurements, the actual stage environment add some important aspects that may affect the profile losses: potential effect from upstream or down-

stream rows, higher free-stream turbulence intensity and wakes from the previous rows. All of these perturbations can affect the boundary layer laminar-to-turbulent transition and may influence how the rough surface affects the losses.

The stage investigated was composed of prismatic rows. The optimized blade geometry used during the experimental campaign was employed for both the stator and the rotor rows. The inlet boundary conditions measured during cascade tests were adopted for the computations (P_t, T_t and Tu), while the back pressure was changed, in order to have an exit Mach number of about 0.50 for both the rows (Tab. 4.2). The stator inlet flow angle was chosen to have nominal incidence on the blade, while the value of the rotational speed assures the same incidence on the rotor row. For the blades axial gap, a typical value employed in a real machine layout was selected (about 0.4 stator C_{ax}). The meridional channel geometry has a constant mean radius, and it is slightly conical in order to ensure the same axial velocity in both the rows (Fig. 4.27). In this way, the mid-span sections of the two blades work at the same conditions as for the cascade tests. Moreover, an aspect ratio of about $AR = 3.2$ and a radius ratio of about $RR = 1.3$ were chosen in order to ensure a two-dimensional flow in these sections. All the runs were performed at the same expansion ratio, while the Reynolds number varies within the range investigated experimentally. Moreover, the same five values of surface roughness tested were taken under consideration.

Three-dimensional viscous unsteady runs were performed, employing a full-annulus approach. Due to the high computational costs of the unsteady runs, stator and rotor blades have the same blade count, resulting in a periodicity domain of 1:1. The number of time-steps was selected after a sensitivity analysis carried out using three different values: 25, 50 and 100. Fifty time-steps per blade passing period ensured the independence of the solutions from time-steps. The O-type grid used for the cascade computations was adopted for the two-row discretization (Fig. 4.24). A summary of computational

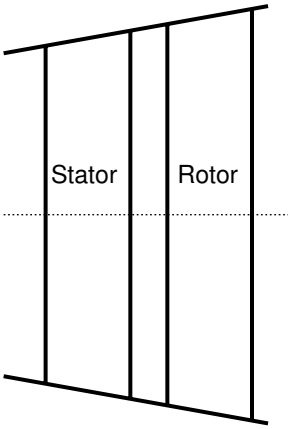

Figure 4.27: **Stage meridional view**

Table 4.5: **Stage data**

Axial gap	$0.4C_{ax}$
Aspect ratio	3.2
Radius ratio	1.3
Periodicity domain	1:1

data of the stage are reported in Table 4.5.

The total pressure loss coefficient at mid-span section of both the stator and the rotor rows were calculated from the time-averaged solution. The data were collected in order to compare the results with the ones obtained for the cascade. The analysis of the results leads to different conclusions for the two rows. Employing the same boundary conditions of the cascade tests, the stator still works as a cascade-like environment. The boundary layer shows a laminar behavior for large part of the suction side even at the higher values of the Reynolds number, in particular for the lower values of k_s/C. Then, as happens for the cascade flow, a transitional behavior

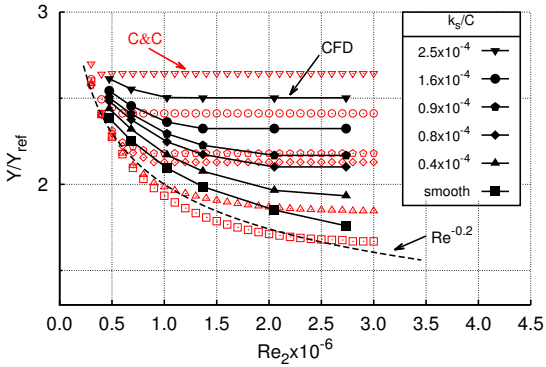

Figure 4.28: **Computed total pressure loss coefficient of rotor row: time-averaged CFD (black filled symbol and solid line) and Craig & Cox correlation (red open symbol) results**

is found for the higher surface roughness and Reynolds number values. For the investigated case, with a subsonic exit flow, the presence of a blade row, which generates a potential field downstream, has a negligible effect on the generation of profile losses. As far as the rotor is concerned, the trend of profile losses depicts a different scenario. The periodic impact of the wakes near the leading edge region of the rotor, promotes the boundary layer transition. Most of the suction side surface is affected by turbulent flow, which results in a higher loss level compared to the steady state cascade environment with attached boundary layer. This behavior is independent of the surface finishing of the blade, and starts from the lower Reynolds investigated. The results of the computations are summarized in Fig. 4.28, where the rotor profile losses are reported as a function of Re_2 for all the five roughness (filled symbol and solid line). In all the cases, the loss trend with respect to Reynolds is very close to the

$Re^{-0.2}$ curve, which represents the loss trend of a turbulent boundary layer. This is the reason why the loss level is about twice the one found with the cascade experimental campaign (Y_ref is the same for the two cases). The figure shows how increasing k_s/C has the main effect of moving the loss curve towards higher values. Moreover, it modifies the value of the threshold Reynolds (Re_{th}) at which the curve leaves the turbulent trend: the higher the roughness, the lower the Re_{th} value. Once the Re_{th} is overcome, increasing Re_2 leads the losses trend towards the fully-rough regime. With respect to the cascade results, the ratio between Y (at highest Re_2 and k_s/C) and Y_{smooth}, is slightly lower, about 1.45. In the same plot the loss coefficients calculated by means of the Craig & Cox correlation (open symbol) are reported. The comparison with the CFD shows a generally good agreement. As for the cascade tests, the correlation predicts an increase of losses in fully-rough regime of $Y/Y_{smooth} \simeq 1.55$. In this case, the computations slightly under predict the roughness effect. Analysing the plot, a slight shift in the absolute value is seen for all the Reynolds and surface finishing computed. In particular, when comparing to Craig & Cox's predictions, the calculations compute a higher loss at the lower k_s/C, and underestimate it at higher ones. But the main difference is in the estimation of Re_{th} and as a consequence, of the Reynolds number at which the fully-rough regime starts. Figure 4.29 shows the time-averaged profile losses as a function of k_s/C for different Reynolds numbers. In light of the previous discussion both the CFD (black filled symbol and solid line) and the Craig & Cox (red open symbol) results show a turbulent nature. In this case, the loss trend does not present the typical "knee" of the transition region, but follows a quite linear trend according to Speidel's [68] results. From this point of view, the comparison between the CFD and the correlative approach is encouraging. In fact, despite the difference in the absolute values, the slope of the curves is in good agreement with the experiments too.

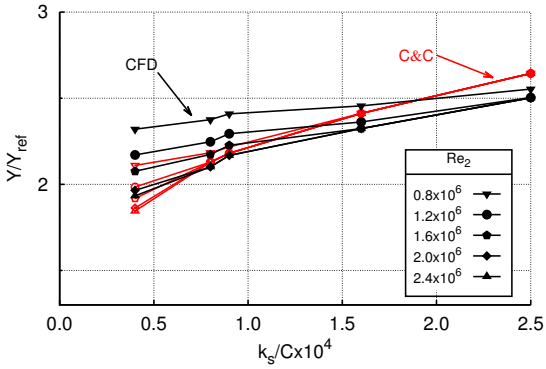

Figure 4.29: **Computed total pressure loss coefficient of rotor row: time-averaged CFD (black filled symbol and solid line) and Craig & Cox correlation (red open symbol) results**

As aforementioned at the beginning of section 4.5, all these results are effective for the original geometry also. The stage environment results have pointed out as, for this type of blading, the effect of surface roughness is to shift the losses curve towards higher values with respect to the smooth blade ones. No potential or upcoming wakes effects are expected to modify the losses curve. This is probably due to the flow conditions, i.e. high Reynolds (about $Re = 1.0\text{x}10^6$) and low exit Mach numbers (lower than $M = 0.5$), whereby these blading are designed. Thus, they would suggest to use the best allowed surface finishing to design the blade. It is reasonable think that the same machining will be employed to manufacture both the blades, thus producing the same roughness over the surface. The optimized blade has a chord slightly greater than the original one, hence it will work at lower Reynolds number and relative roughness with a further reducing of the profile loss. This further gain in performance is probably of

an order of magnitude lower than the one found with the optimization. For these reasons, the results obtained with the optimization and confirmed by cascade tests, are effective irrespective of the surface finishing adopted.

Chapter 5

CFD verification of optimized stage

This chapter discusses the results of the post-optimization assessment, in order to address the new stage industrialization and the fine tuning of preliminary design tools. The main sources of loss were investigated by means of CFD calculations. The analyses were performed in different geometrical configurations from the one employed during the optimization.

5.1 Computational framework

An exhaustive comparison between the performance of the original and optimized geometries was carried out. The analysis was aimed at independently investigating the effects of profile loss, secondary flows and tip clearance on the stage efficiency, pointing out the differences in the aerodynamic behavior of the two geometries. The parametric study included geometrical features such as stagger angle (ξ), aspect ratio (AR) and radius ratio (RR) and was extended in a wide range of flow coefficient (ϕ) to cover the expected operating space.

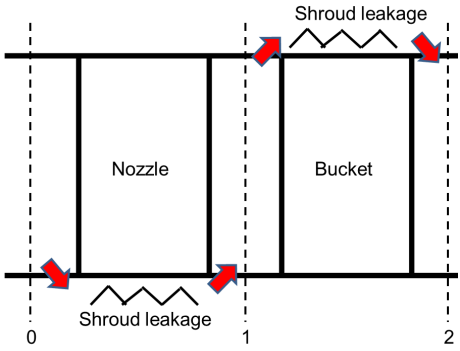

Figure 5.1: **Scheme of the meridional flow path geometry and shroud leakages position**

A cylindrical flow path geometry was selected (Figure 5.1), to avoid local three-dimensional effects that can hide the actual impact of the parameter under investigation. For each configuration, a performance curve was drawn by varying the stage back pressure only, while keeping the same total pressure and temperature distribution at stage inlet. Three-dimensional viscous CFD run were performed by means of Wilcox's two-equation k-ω high-Reynolds model for the turbulence closure, and imposing the hydraulically smooth surface hypothesis. Moreover, suitable repeating boundary conditions were adopted in order to mimic the repeating stage environment whereby these blading are thought. Finally, the leakage model was not included into the computations when the effect of profile and secondary losses were studied.

5.2 Impact of profile loss

The impact of the profile loss on the efficiency of the two stages was studied by varying the stagger angle of the blade.

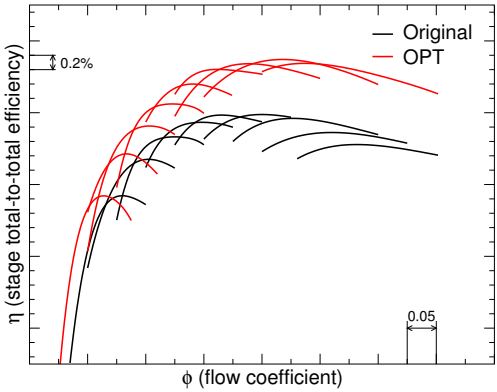

Figure 5.2: **Comparison between original and OPT performance curves at different stagger angles (constant AR, RR, Re_C)**

Both stages employ prismatic blades, use a single airfoil for stator and rotor rows, and are designed to work with an optimum pitch-to-chord ratio at blade midspan. The only geometrical feature that can affect the profile loss, with a fixed blade size and flow path geometry, is the stagger angle. In fact, restaggering the blade changes the position of the working line in the ϕ-ψ chart, modifying the deflection undergone by the fluid, the loading of the airfoil and, as a consequence, the aerodynamic performance.

The computations were performed in a cylindrical flow path characterized by high AR (about $AR/AR_{ref} = 1.0$) and low RR (about $RR/RR_{ref} = 1.08$), in order to limit the influence region of the secondary flows near the endwalls. In this way, the evaluation of the midspan loss was not affected by secondary flows. The results of such an analysis are summarized in Figure 5.2. Here the performance curves in terms of total-to-total efficiency, for each stagger value, are reported for both geometries investigated. Both stages show a generally

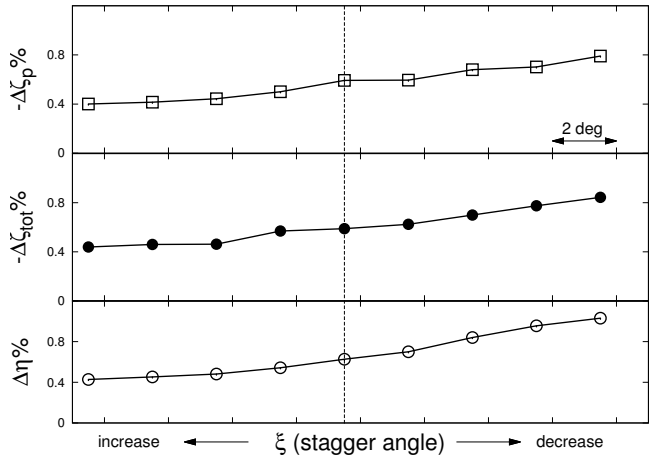

Figure 5.3: **Comparison between delta-efficiency and delta-loss coefficients at different stagger angles (constant** AR, RR, Re_C**)**

good off-design behavior for all the stagger angles, revealing a good robustness to incidence, even though the OPT geometry exhibits a slightly sharper leading edge. Moreover, the picture highlights that the envelope curve of the peak efficiency for the OPT has always a greater efficiency. This ensures a higher stage efficiency when the OPT stage is employed instead of the original, whatever the design point of the machine is. The increase in the efficiency gain, with a rather linear trend towards the high flow coefficients, is due to the different position of the peak efficiency of the envelope curve. Figure 5.3 shows the trend of $\Delta\eta$ with stagger angle, evaluated for two curves at the same working line. The picture points out the almost linear trend of increasing the efficiency towards the lower stagger values, from about 0.45% to 1.0%. A similar consideration can be drawn, always from Figure 5.3, regarding $\Delta\zeta_{tot}$ and $\Delta\zeta_p$. The total loss coefficient was evaluated

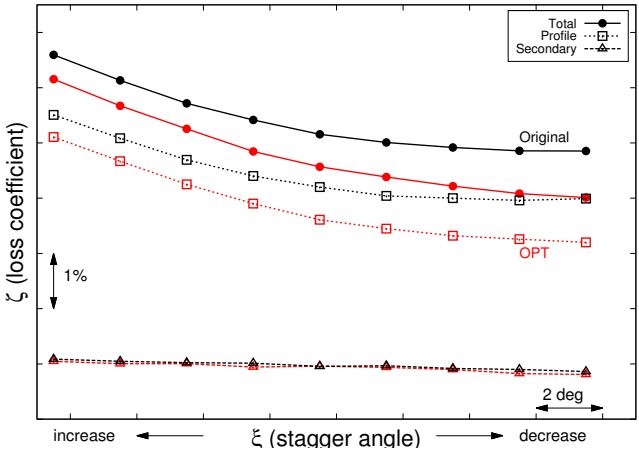

Figure 5.4: **Total, profile and secondary loss coefficients at different stagger angles: comparison between original and OPT (constant AR, RR, Re_C)**

making a balance between the inlet and the outlet section of the computational domain, while the profile loss was calculated at the blade midspan. Both are evaluated by means of equation (5.1). The difference between these two coefficients, in absence of leakage flows, provides the amount of secondary losses (5.2).

$$\zeta = 1 - \left(\frac{c_2}{c_{2is}}\right)^2 \tag{5.1}$$

and

$$\zeta_{sec} = \zeta_{tot} - \zeta_p \tag{5.2}$$

As far as efficiency is concerned, the comparison was done between two curves at the same working line. The trends of the loss coefficients are similar to the efficiency ones. Observing the profile losses, it is worth noting that the benefits of the OPT rise towards the reduced staggers, as previously found

by analyzing the trend of the efficiency curves. This consideration highlights that only the aerodynamic performance of the airfoil guides the $\Delta\eta$, revealing that both stages have a similar behavior in terms of secondary flows. Figure 5.4 confirms this result, showing total, profile and secondary loss coefficient (ζ_{sec}) of original and OPT, at different stagger positions. The picture shows how the impact of secondary loss is almost constant in the whole range of stagger, or presents a slight increases when the stagger, as well as the fluid deflection, increases. The trend is the same for the two airfoils and has similar absolute value.

5.3 Impact of secondary flows

Secondary flows effects on the aerodynamic performance of the two stages were studied at three different stagger angles, by varying independently the blade aspect ratio and radius ratio of the meridional flow path. The three stagger values were selected in order to compare the geometries along the same working line in the $\phi - \psi$ chart.

First, the impact of aspect ratio was investigated at four different values. In order to preserve the same Reynolds number based on blade chord (Re_C), the blade height was varied at a fixed chord length. For each AR, a flow path geometry with a different mean diameter was selected, in order to keep the radius ratio unchanged (constant value $RR/RR_{ref} = 1.08$). Moreover, the blade speed was modified to preserve the kinematic similitude of the stage at midspan. The results of the computations are summarized in Figure 5.5, where the peak efficiency, calculated at different AR, is reported for both stages at three different stagger angles. The computations confirm the well-known trend, whereby reducing AR increases the blade span influenced by the secondary flows, thus reducing the efficiency. The efficiency gain is nearly constant for varying the aspect ratio, as seen in Figure 5.5. A slight reduction in the gain is observed at higher stagger and

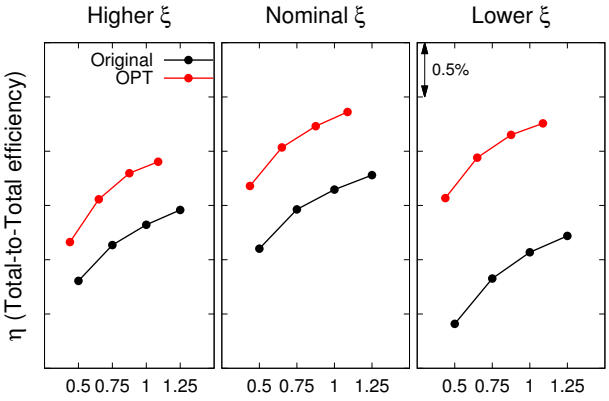

Figure 5.5: **Aspect ratio effect for three values of stagger angle: comparison in terms of peak efficiency values (constant RR, Re_C)**

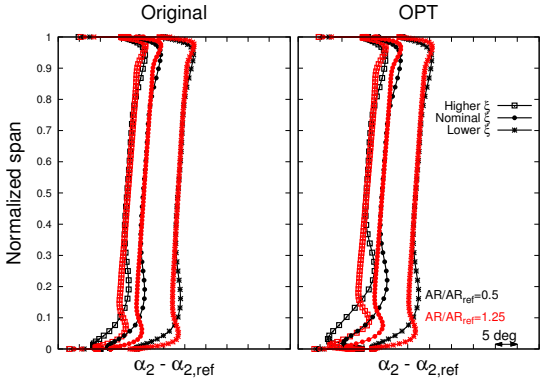

Figure 5.6: **Aspect ratio effect: spanwise distribution of swirl angles at bucket exit, for several stagger angles (constant RR, Re_C)**

lower aspect ratios. This is due to the different leading edge geometries, nominal stagger angles and isentropic Mach number distributions over the blade surface of the two airfoils. These cause an increase in loading in the front part of the OPT airfoil that slightly intensifies the secondary flows, in particular at higher stagger when the blade loading is higher. Overall, the two stages exhibit similar secondary flows intensity and depth of penetration into the main stream, as shown in Figure 5.6. Here the span-wise distribution of swirl angles at the bucket exit, is reported for several stagger angles. The picture shows the evolution of the over- and under-turning in the endwalls region due to passage vortex, and how the secondary flows increase their penetration with reduced AR and higher stagger angles, affecting the aerodynamic performance of the stage. The percent of the blade height influenced by these flows is almost the same for both the stages. This is true even if $\Delta\alpha_2$ is slightly greater for OPT, in particular for higher stagger at $AR/AR_{ref} = 0.5$ as mentioned for Figure 5.5. Due to repeating stage boundary conditions, the same considerations drawn for the bucket are true for the nozzle, even if the distribution of blade-to-blade exit angles are quite different.

As far as the radius ratio analysis is concerned, four different values were investigated. The computations were performed with different flow path geometries and blade speeds in order to preserve the aspect ratio (fixed value $AR/AR_{ref} = 0.75$) and the kinematic similitude of the stage at midspan, for each RR. The results are summarized in Figure 5.7, where the peak efficiency, calculated at various RR, is reported for both stages at three different stagger angles. Increasing the radius ratio increases the variation of the inlet flow angle. The blade operates with a very different incidence angle from hub to tip, while the midspan works in every configuration in the same way. Thus the endwalls regions work in very off-design conditions. For these reasons the efficiency is progressively reduced when the radius ratio is increased, as shown in Fig-

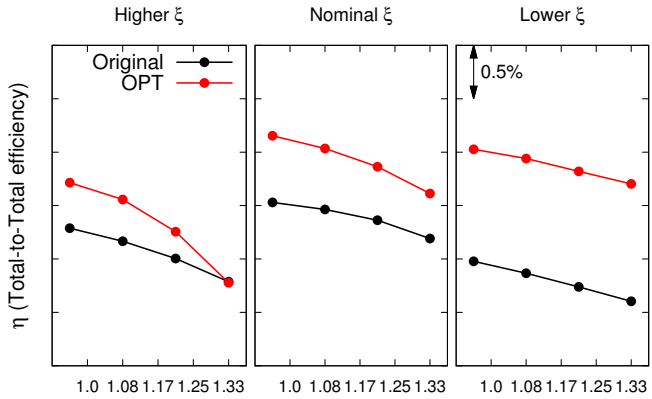

Figure 5.7: **Radius ratio effect for several values of stagger angle: comparison in terms of peak efficiency values (constant AR, Re_C)**

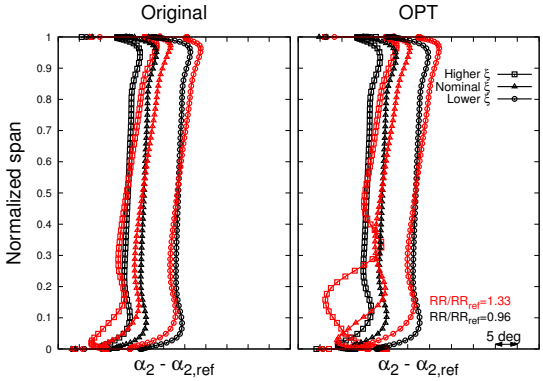

Figure 5.8: **Radius ratio effect: spanwise distribution of swirl angles at bucket exit, for several stagger angles (constant AR, Re_C)**

ure 5.7. Figure 5.7 also shows that the radius ratio strongly impacts the efficiency gain, reducing $\Delta\eta$ for the more three-dimensional configurations. In particular, the effect becomes more intense at higher stagger angles, until the gain is nullified. As discussed for the aspect ratio investigations, once again the reason is linked to the different leading edge geometries, nominal stagger angles and isentropic Mach number distributions over the blade surface of the two airfoils. In this case, the impact is augmented from the greater incidence variation, which affects more the OPT airfoil. Figure 5.8 shows the span-wise distribution of swirl angles at the bucket exit, for several stagger angles. When comparing the two stages, a similar angle distribution can be observed for the lower radius ratio, as well as the same penetration of the secondary flows in the mainstream. In this case, the stagger effect is limited, and the over- and under-turning of the flow are confined near the endwalls regions. Different considerations have to be made for the case $RR/RR_{ref} = 1.33$. The impact of secondary flows is stronger for the OPT stage, and more marked at the higher stagger. In fact, secondary flows grow up to affect about 40% of the blade height, causing the efficiency reduction previously discussed.

The effect shown in Figure 5.8 is also displayed in Figures 5.9 and 5.10, where the entropy contours downstream of the OPT bucket are shown for $RR/RR_{ref} = 0.96$ and $RR/RR_{ref} = 1.33$. In Figure 5.9, it can be noted for both stagger angles the trace of the blade wake and the entropy generated from the endwalls corner vortices. Moreover, the wide loss region due to the passage vortex and the trailing edge shed vorticity (or the vorticity generated within the blade passage near the suction side induced by the passage vortex) is shown. Analyzing both figures, it is confirmed that the higher stagger configurations exhibit a wider trace of the blade wake and a wider flow region affected by secondary flows: as a consequence the efficiency is reduced. In particular, the secondary flows region grows as the stagger and radius

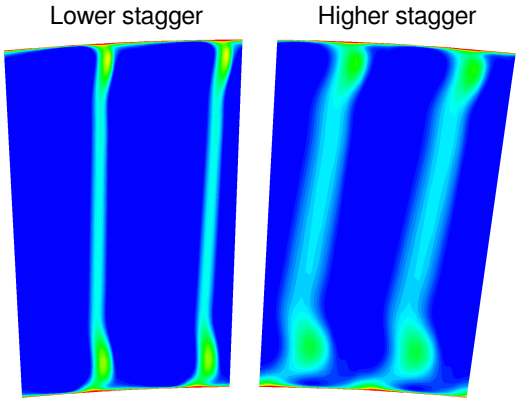

Figure 5.9: **Entropy contours at 0.4 C_{ax} downstream the OPT bucket trailing edge** ($RR/RR_{ref} = 0.96$)

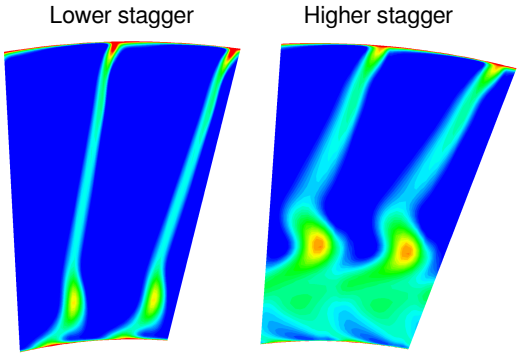

Figure 5.10: **Entropy contours at 0.4 C_{ax} downstream the OPT bucket trailing edge** ($RR/RR_{ref} = 1.33$)

ratio increase, filling about 40% of the blade height (higher stagger and $RR/RR_{ref} = 1.33$), and producing an intensive mixing and hence a high level of losses. The hub region is the one where the impact of secondary flows is most significant and most of losses are generated. This is due to the higher positive incidence whereby the blade operates and leads to the growth of these flows. Similar observations can be found in Benner et al. [72] and Perdichizzi and Dossena [73].

5.4 Impact of shroud leakages

When dealing with stage performance predictions, the impact of shroud leakages can not be neglected. In the present study, the shroud leakages were included into the computations by means of the shroud model previously described. The scheme of Figure 5.1 shows where the shrouds were placed into the computational domain. Figure 5.11 shows the CFD results

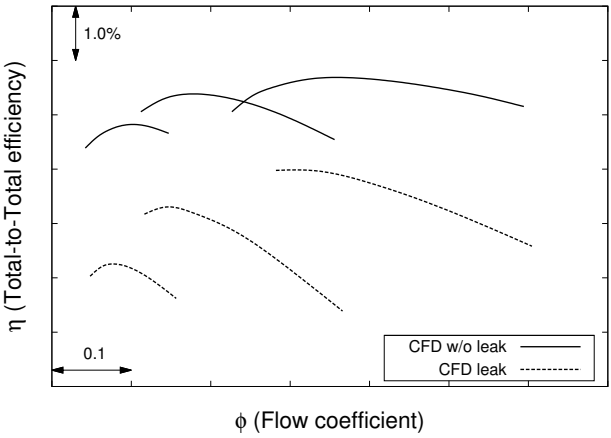

Figure 5.11: **Impact of shroud leakages on stage performance**

performed for the OPT stage at three different stagger angles, with and without including shroud leakages. Two main effects can be pointed out: the reduction in efficiency and the shift of the peak efficiency towards reduced flow coefficients. The first aspect is due to the penetration of the leakage flow into the mainstream, which perturbs the flow in the endwalls region enhancing the mixing losses and affecting the next row performance. As a result, an efficiency drop proportional to the leakage mass flow rate is expected, as found by Rosic et al. [42] in their work. The second aspect is due to the growing impact that the leakage flows have with the increase of blade loading, that causes a greater efficiency drop at higher work coefficients, according to the Kacker and Okapuu formulation for shrouded blades [74].

For the two blades under investigation, the seals have the same geometry, therefore the comments made for the OPT geometry still hold for the original one. The leakage mass flow rate is driven by the pressure drop across the blade. Thus, due to the greater blade loading, a higher leakage mass flow is expected for the OPT airfoil with respect to the original one. As a consequence, the efficiency increase obtained without including the shroud model is reduced, by about an amount equal to the difference of leakage mass flow.

The analysis of the main sources of loss has pointed out that the two airfoils behave in a similar way from an aerodynamic point of view. For the basic two-dimensional loss, the results show the important role played by the stagger angle for this type of blading, having a strict link with the profile loss. The re-staggering moves the stage working line in a wide operating space, drawing a set of different performance curves. It is the shape of the envelope of these curves that guides the trend in efficiency gain, which is linked to the aerodynamic behavior of the airfoil geometry. The secondary flows analysis shows that both geometries have a similar aerodynamic behavior when these flows are confined to the endwalls regions (high aspect ratio), and the span-wise

variation of inlet flow angle is reduced (low radius ratio): for these cases the efficiency gain remains about constant. Different results were found in the more three-dimensional flow field, where the performance of the OPT stage decay more quickly then the original ones, leading to a reduction in the efficiency gain. Finally, the shroud leakages investigation has introduced another penalty for the OPT stage. The greater blade loading, together with the same seal geometry, causes a major stage leakage mass flow. Thus, an increased efficiency drop, equal to the difference of leakage mass flow between the two geometries, is expected.

All these results are useful for the stage industrialization, addressing the preliminary design tools modifications. This means not only acts on the improvement of the performance prediction capability, but also on the design rules which compound the overall design chain. Generally the prediction capability relies on a correlative approach, exploiting empirical expressions to predict the performance of each component, addressing aerodynamic as well as mechanical design, in same cases. The high maturity level of CFD computations can play an important role in replacing lengthy and costly experimental campaigns with numerical simulations. Thus allowing the fine-tuning of the used correlative approach and proving its reliability. As far as the design rules is concerned, these results can be transformed in practical design rules and guide the designer in to select the better trade-off for the machine layout: for example which meridional channel geometry employ and in which operating point the stage should work.

Summary and conclusions

In this PhD thesis, a redesign strategy for high-pressure steam turbine stages was described in detail. The procedure was applied to an industrial problem concerning the redesign of a reaction stage for steam turbine drums. Each step of the strategy was critically analysed in order to point out advantages, drawbacks, and the implications that any designer's choice has on the final result.

The attention was mainly focused on the optimization technique which relies on a response surface method, coupling the high-fidelity CFD RANS computations with an optimization algorithm based on meta-models. In particular, two of these models were presented and analysed in depth: the support vector machines and the artificial neural networks. A parametric analysis was carried out in order to choose the better training parameters combination for each model, thus allowing its best prediction capability. The comparison between SVM and ANN has proved their reliability in approximating the response surface of the problem, making them effective and suitable for multi-objective optimization problems. For the present optimization, the SVM approach was preferred to the ANNs one, due to the better accuracy whereby has learned the links between parameters and objective functions/constraints. As a result, the final geometry,

selected as optimum of the problem, observes all the imposed constraints and ensures an efficiency increase between 0.5% and 1.25% depending on the operating conditions.

In order to address the product industrialization, the effect of surface roughness and the losses associated with profile, secondary flows, and leakages mass flow were investigated in depth. The discussion of the effects of surface roughness has put in light the importance of cascade experimental campaigns in providing data to fine-tune the computational models, and at the same time the limits of such approach in to mimic the real machine environment. As far as the analysis of the main sources of loss is concerned, the results have highlighted which parameters affect mainly each of these source of losses, put in light on which aspects the optimization has pushed to yield the efficiency increase required. However, the goal of this analysis was to transform the numerical results in practical design rule, in order to update the preliminary design tools and to address the design of the new machine.

Overall, the proposed strategy has proved to be a robust and flexible tool to use for multi-objective and multidisciplinary redesign problems. It reduces time and costs, while preserving competitiveness. Therefore, it offers a valid and accurate approach to meet the industrial requirements to design new highly efficient and reliable machines.

Bibliography

[1] Chen, B., and Yuan, X., 2008. "Advanced aerodynamic optimization system for turbomachinery". *ASME Journal of Turbomachinery,* ***130***(1), p. 021005.

[2] Burguburu, S., Toussaint, C., Bonhomme, C., and Leroy, G., 2004. "Numerical optimization of turbomachinery bladings". *ASME Journal of Turbomachinery,* ***126***, pp. 91–100.

[3] Checcucci, M., Sazzini, F., Marconcini, M., Arnone, A., Coneri, M., Franco, L. D., and Toselli, M., 2011. "Assessment of a neural-network-based optimization tool: a low specific-speed impeller application". *International Journal of Rotating Machinery,* ***2011, Number ID8175471***, pp. 1–11.

[4] Pritchard, L. J., 1985. "An eleven parameter axial turbine airfoil geometry model". In Gas Turbine Conference and Exhibit, 18-21 March, Houston, Texas, no. 85-GT-219.

[5] Rubechini, F., Schneider, A., Arnone, A., Daccà, F., Canelli, C., and Garibaldi, P., 2011. "Aerodynamic redesigning of an industrial gas turbine". In ASME Turbo Expo, 6-10 June, Vancouver, BC, Canada, no. GT2011-46258.

[6] Bonaiuti, D., Arnone, A., Ermini, M., and Baldassarre, L., 2006. "Analysis and optimization of transonic centrifugal compressor impellers using the design of experiments technique". *ASME Journal of Turbomachinery,* ***128***(1), pp. 786–797.

[7] Leung, T. M., and Zingg, D. W., 2012. "Aerodynamic shape optimization of wings using a parallel newton-krylov approach". *AIAA Journal,* ***50***(3), pp. 540–550. March.

[8] Van den Braembussche, R. A., Alsalihi, Z., Verstraete, T., Matsuo, A., Ibaraki, S., Sigumoto, K., and Tomita, I., 2012. "Multidisciplinary multipoint optimization of a transonic turbocharger compressor". In ASME Turbo Expo, 11-15 June, Copenaghen, Denmark, no. GT2012-69645.

[9] Ellbrant, L., Eriksson, L. E., and Martensson, H., 2012. "Desing of compressor blades considering efficiency and stability using cfd based optimization". In ASME Turbo Expo, 11-15 June, Copenaghen, Denmark, no. GT2012-69272.

[10] Chahine, C., Seume, J. R., and Verstraete, T., 2012. "The influence of metamodeling techniques on the multidisciplinary design optimization of a radial compressor impeller". In ASME Turbo Expo, 11-15 June, Copenaghen, Denmark, no. GT2012-68358.

[11] Seo, D.-H., Roh, T.-S., and Choi, D.-W., 2009. "Defect diagnostics of gas turbine engine using hybrid svm-ann with module system in off-design condition". *Journal of Mechanical Science and Technology,* ***23***, pp. 677–685.

[12] Lu, W.-Z., and Wang, W.-J., 2005. "Potential assessment of the "support vector machine" method in forecasting ambient air pollutant trends". *Chemospere,* ***59***, pp. 693–701.

[13] Adamkon, M. M., and Cheriet, M., 2009. "Model selection for the ls-svm. application to handwriting recognition". *Pattern Recogn.,* ***42***(12), pp. 3264–3270.

[14] Anguita, D., Cravero, C., Filz, C., and Rivieccio, F., 2003. "An innovative technique for the aerodynamic design of turbine blade profiles using artificial intelligence". In Proc. of the 33rd AIAA Fluid Dynamics Conference, Orlando, Florida, 23-26 June.

[15] Pierret, S., and van den Braembussche, R. A., 1999. "Turbomachinery blade design using a navier-stokes solver and artificial neural network". *ASME Journal of Turbomachinery,* ***121***, pp. 326–332.

[16] Rubechini, F., Schneider, A., Arnone, A., Cecchi, S., and Garibaldi, P., 2012. "A redesign strategy to improve the efficiency of a 17-stage steam turbine". *ASME Journal of Turbomachinery,* ***134***(3), p. 031021.

[17] Suykens, J. A. K., Brabanter, J. D., Lukas, L., and Vandewalle, J., 2002. "Weighted least squares support vector machines: robustness and sparse approximation". *Neurocomputing,* ***48***, pp. 85–105.

[18] Suykens, J. A. K., Gestel, T. V., Brabanter, J. D., Moor, B. D., and Vandewalle, J., 2002. *Lest Squares Support Vector Machines*. World Scientific, Singapore.

[19] Valyon, J., and Horvth, G., 2005. "A robust ls-svm regression". In IEC (Prague), C. Ardil, ed., pp. 148–153.

[20] Vapnik, V., 1998. *Statistical learning theory*. Wiley.

[21] Vapnik, V. N., 1999. *The nature of statistical learning theory*, 2nd ed. Springer, Berlin.

[22] Burges, C. J., 1998. "A tutorial on support vector machines for pattern recognition". *Data Mining and Knowledge Discovery,* ***2***, pp. 121–167.

[23] Smola, A. J., and Schölkopf, B., 2004. "A tutorial on support vector regression". *Statistics and Computing,* ***14***(3), Aug., pp. 199–222.

[24] Cherkassky, V., and Ma, Y., 2004. "Practical selection of svm parameters and noise estimation for svm regression". *Neural Networks,* ***17***, pp. 113–126.

[25] Mazzetti, A., 1991. *Reti Neurali Artificiali.* Apogeo editrice informatica, Milano.

[26] Haykin, S., 1999. *Neural Networks, A Comprehensive foundation*, 2 ed. Prentice Hall, New Jersey.

[27] Cichocki, A., and Unbehauen, R., 1994. *Neural Networks for Optimization and Signal Processing.* Wiley, New York.

[28] Perrone, M. P., and Cooper, L. N., 1992. When networks disagree: Ensemble methods for hybrid neural networks. Institute for brain and neural system, physics department and neuroscience department, providence, Brown University, 27 October.

[29] Arnone, A., 1994. "Viscous analysis of three-dimensional rotor flow using a multigrid method". *ASME Journal of Turbomachinery,* ***116***(3), pp. 435–445.

[30] Arnone, A., 1995. *Multigrid Methods for Turbomachinery Navier–Stokes Calculations.* in Solution Techniques for Large–Scale CFD Problems Lausanne. W.G. Habashi, Ed., John Wiley & Sons.

[31] Jameson, A., Schmidt, W., and Turkel, E., 1981. "Numerical solutions of the euler equations by finite volume method using runge–kutta time–stepping schemes". In AIAA paper 81-1259, 14^{th} Fluid and Plasma Dynamics Conference, June 23-25, Palo.

[32] Swanson, R., and Turkel, E., 1992. "On central-difference and upwind schemes". *Journal of Computational Physics,* ***101***, pp. 292–306.

[33] Baldwin, B. S., and Lomax, H., 1978. "Thin layer approximation and algebraic model for separated turbulent flows". In AIAA paper 78-257, 16^{th} Aerospace Sciences Meeting, January 16-18, Huntsville, AL, USA.

[34] Spalart, P. R., and Allmaras, S. R., 1994. "A one-equation turbulence model for aerodynamic flows". *La Recherche Aèrospatiale,* ***1***, pp. 5–21306.

[35] Wilcox, D. C., 1998. *Turbulence Modeling for CFD*, 2^{nd} ed. DCW Ind. Inc., La Cañada, CA, USA. ISBN 1-928729-10-X.

[36] Pacciani, R., Marconcini, M., Fadai-Ghotbi, A., Lardeau, S., and Leschziner, M. A., 2011. "Calculation of high-lift cascades in low pressure turbine conditions using a three-equation model". *ASME J. Turbomach.,* ***133***(3), July, p. 031016.

[37] Mayle, R. E., and Schultz, A., 1997. "The path to predicting bypass transition". *ASME J. Turbomach.,* ***119***(3), July, pp. 405–411.

[38] Pacciani, R., Marconcini, M., Arnone, A., and Bertini, F., 2011. "An assessment of the laminar kinetic energy concept for the prediction of high-lift, low-Reynolds number cascade flows". *Proc. I. Mech. E. Part A: Journal of Power and Energy,* ***225***(7), pp. 995–1003.

[39] Wilcox, D. C., 2008. "Formulation of the $k-\omega$ turbulence model revisited". *AIAA J.,* ***46***(11), November, pp. 2823–2838.

[40] Wallis, A. M., Denton, J. D., and Demargne, A. A. J., 2001. "The control of shroud leakage flows to reduce

aerodynamic losses in a low aspect ratio, shrouded axial flow turbine". *Journal of Turbomachinery,* ***123***(2), pp. 334–341.

[41] Pfau, A., Kalfas, A. I., and Abhari, R. S., 2007. "Making use of labyrinth interaction flow". *Journal of Turbomachinery,* ***129***(1), pp. 164–174.

[42] Rosic, B., Denton, J. D., and Curtis, E. M., 2007. "The influence of shroud and cavity geometry on turbine performance – an experimental and computational study, Part 1: Shroud Geometry". In ASME Turbo Expo, 14-17 May, Montreal, Canada, no. GT2007-27769.

[43] Rosic, B., Denton, J. D., and Pullan, G., 2006. "The importance of shroud leakage modelling in multistage turbine flow calculations". *Journal of Turbomachinery,* ***128***(4), pp. 699–707.

[44] Rubechini, F., Marconcini, M., Arnone, A., Cecchi, S., and Daccà, F., 2007. "Some aspects of cfd modeling in the analysis of a low-pressure steam turbine". In ASME Turbo Expo, 14-17 May, Montreal, Canada, no. GT2007-27235.

[45] McGreeham, W. F., and Ko, S. H., 1989. "Power dissipation in smooth and honeycomb labyrinth seals". In ASME Turbo Expo, 5-8 June, Toronto, Canada, no. 89-GT-220.

[46] Dossena, V., Perdichizzi, A., and Savini, M., 1999. "The influence of endwall contouring on the performance of a turbine nozzle guide vane". *ASME Journal of Turbomachinery,* ***121***(2), p. 200.

[47] D'Ippolito, G., Dossena, V., and Mora, A., 2011. "The influence of blade lean on straight and annular turbine cascade flow field". *ASME Journal of Turbomachinery,* ***133***, p. 011013.

[48] Nikuradse, J., 1933. "Laws for flows in rough pipes". *VDI-Forchungsheft 361, Series B,* ***Vol. 4***. (English translation NACA TM 1292, 1950).

[49] Schlichting, H., 1936. "Experimentelle Untersuchungen zum Rauhigkeitsproblem". In Ingenieur-Archive 7, 1 bis 34.

[50] Bons, J. P., 2010. "A review of surface roughness effects in gas turbines". *ASME Journal of Turbomachinery,* ***132***, p. 021004.

[51] Flack, K. A., and Schultz, M. P., 2010. "Review of hydraulic roughness scales in the fullu rough regime". *ASME Journal of Fluid Engineering,* ***132***, p. 041203.

[52] Schlichting, H., 1979. *Boundary-Layer Theory*, 7$^{\text{th}}$ ed. McGraw–Hill, Inc., New York. ISBN 0-07-055334-3.

[53] Speidel, L., 1962. "Determination of the necessary surface quality and possible losses due to roughness in steam turbines". *Elektrizitätswirtschaft,* ***61***(21), pp. 799–804.

[54] Hummel, F., Lötzerich, M., Cardamone, P., and Fottner, L., 2005. "Surface roughness effects on turbine blade aerodynamics". *ASME Journal of Turbomachinery,* ***127***, pp. 453–461.

[55] Dirling, R. B., 1973. "A method for computing roughwall heat transfer rates on re-entry nosetips". *AIAA paper 73-763.*

[56] Sigal, A., and Danberg, J. E., 1990. "New correlation of roughness density effect on the turbulent boundary layer". *AIAA Journal,* ***28***(3), pp. 554–556.

[57] van Rij, J. A., Belnap, B. J., and Ligrani, P. M., 2002. "Analysis and experiments on three-dimensional, irregular surface roughness". *ASME Journal of Fluids Engineering,* ***124***, pp. 671–677.

[58] Waigh, D. R., and Kind, R. J., 1998. "Improved aerodynamic characterization of regular three-dimensional roughness". *AIAA Journal,* ***36***(6), pp. 1117–1119.

[59] Zhang, Q., Goodro, M., Ligrani, P. M., Trindade, R., and Sreekanth, S., 2006. "Influence of surface roughness on the aerodynamic losses of a turbine vane". *ASME Journal of Turbomachinery,* ***128***, pp. 568–578.

[60] Im, J. H., Shin, J. H., Hobson, G. V., Song, S. J., and Millsaps, K. T., 2013. "Effect of leading edge roughness and Reynolds number on compressor profile loss". In ASME Turbo Expo, June 3-7, San Antonio, TX, USA, no. GT2013-95487.

[61] Vázquez, R., and Torre, D., 2013. "The effect of surface roughness on efficiency of low pressure turbines". In ASME Turbo Expo, June 3-7, San Antonio, TX, USA, no. GT2013-94200.

[62] Hodson, H. P., and Howell, R. J., 2005. "The role of transition in high-lift low-pressure turbines for aeroengines". *Prog. Aerosp. Sci.,* ***41***, pp. 419–454.

[63] Boyle, R. J., 1994. "Prediction of surface roughness and incidence effects on turbine performance". *ASME Journal of Turbomachinery,* ***116***, pp. 745–751.

[64] Mesbah, M., Arts, T., Simon, J. F., and Geuzaine, P., 2009. "Numerical and experimental analysis of surface roughness effects for compressor blades". In AIAA Conference, no. ISABE-2009-1151.

[65] Boyle, R. J., and Senyitko, R. G., 2003. "Measurements and predictions of surface roughness effects on turbine vane aerodynamics". In ASME Turbo Expo, 16-19 June, Atlanta, GA, no. GT2003-38580.

[66] Cebeci, T., and Chang, K., 1978. "Calculation of incompressible rough-wall boundary layer flows". *AIAA Journal,* ***16***(7), pp. 730–735.

[67] Mayle, R. E., 1991. "The role of laminar-turbulent transition in gas turbine engines". *ASME Journal of Turbomachinery,* ***113***, pp. 509–537.

[68] Speidel, L., 1954. "Einfluβ der Oberflächenrauhigkeit auf die Strömungsverluste in ebenen Schaufelgittern". In Forschg, Ing.-Wes. 20, 129-140.

[69] "Feindt, E. G.".

[70] Craig, H. R. M., and Cox, H. J. A., 1970. "Performance estimation of axial flow turbines". In Proceedings of the Institution of Mechanical Engineers, June, Vol. 185, pp. 407–424.

[71] Aungier, R. H., 2006. *Turbine Aerodynamics: Axial-Flow and Radial Inflow Turbine Design and Analysis.* ASME Press, New York.

[72] Benner, M. W., Sjolander, S. A., and Moustapha, S. H., 2004. "Measurements of secondary flows downstream of a turbine cascade at off-design incidence". In ASME Turbo Expo, 14-17 June, Vienna, Austria, no. GT2004-53786.

[73] Perdichizzi, A., and Dossena, V., 1993. "Incidence angle and pitvh-chord effects on secondary flows downstream of a turbine cascade". *ASME Journal of Turbomachinery,* ***115***(3), pp. 383–391.

[74] Kacker, S. C., and Okapuu, U., 1982. "A mean line prediction method for axial flow turbine efficiency". *ASME Journal of Engineering for Power,* ***104***, pp. 111–119.